Modeling complex motility patterns for autophoretic microswimmers

Anupriya Dutta Roy,[1, *] Smita S. Sontakke,[2] Arvind Kumar,[3] Ranabir Dey,[2, †] and Anupam Gupta[1, ‡]

[1]*Department of Physics,*
Indian Institute of Technology Hyderabad, Kandi, Sangareddy 502285, India
[2]*Department of Mechanical and Aerospace Engineering,*
Indian Institute of Technology Hyderabad, Kandi, Sangareddy 502285, India
[3]*Center for Interdisciplinary Programs,*
Indian Institute of Technology Hyderabad, Kandi, Sangareddy 502285, India

ABSTRACT

Symmetry breaking is essential for biological microswimmers to achieve locomotion in viscous environment. Such asymmetry inherent in the swimming mechanism enables the generation of directional forces that overcome fluid resistance, supporting efficient movement and complex interactions. As a synthetic analogue, autophoretic microswimmers, such as isotropic active colloids and active droplets, undergo spontaneous symmetry-breaking of a chemical species that generates interfacial flows which in turn drive persistent self-propulsion. A major complexity in modeling such autophoretic microswimmers stems from the fact that the evolution of the chemical concentration and the flow fields around the microswimmer are coupled by the non-linear advective transport of the chemical species. In this work, we propose a new numerical simulation framework for modeling isotropic autophoretic microswimmers whose propulsion arises solely from self-generated chemical gradients without any built-in geometric or chemical anisotropy. The proposed numerical framework is based on a high-accuracy pseudospectral method that resolves the full, coupled advection–diffusion–Stokes equations without any prescribed slip formula. Slip velocities emerge self-consistently from instantaneous concentration gradients at the particle surface, which then drive propulsion, and create a disturbance in the domain through a stresslet representation of force and torque free microswimmers. This approach captures nonlinear advection, chemo-hydrodynamic feedback, and many-particle interaction in a single framework. We also show that the proposed numerical framework can capture the intricate chemo-hydrodynamic interactions that lead to emergent complex motility patterns in autophoretic microswimmers, such as disordered swimming with increasing viscosity of the swimming medium and pairwise interactions guided by chemotactic avoidance. At each step, we compare the predictions from our numerical framework with the observations from independently performed experiments using active droplets as a model system for an autophoretic microswimmer.

I. INTRODUCTION

Over the years, synthetic microswimmers have emerged as autonomous agents for executing intricate tasks, like metal ion detection and collection [2], targeted drug delivery [43, 56], assisted fertilization [6], and water remediation [49]. The design and function of these micro/nano-machines often draw direct inspiration from microorganisms, which in turn have evolved sophisticated strategies to achieve efficient propulsion in complex environment [20]. While engineered microswimmers can be actuated by external fields, such as electric [26, 27], magnetic [58, 94], or optical stimuli [5], the practical implementation of such methods faces significant hurdles stemming from miniaturization constraints, fabrication complexity, and diminished performance outside of controlled laboratory settings [16, 42]. In contrast, chemically active microswimmers offer a self-sustained alternative by converting chemical free energy directly into autonomous motion without requiring any external actuation [4, 57, 62, 67]. Their propulsion arises either from phoretic mechanisms, like self-diffusiophoresis or self-electrophoresis (as in Janus microswimmers) [37, 74, 88, 97], or solubilization (as in active droplets) [29, 39, 75, 93, 95], whereby interfacial chemical interactions create gradients in chemical concentration or surface tension which trigger interfacial flow. Once the interfacial flow sets in, the particle self-propels in order to satisfy the non-intertial (zero net hydrodynamic force) constraints of the low Reynolds number regime. Note here that for a Janus-type microswimmer, a material (chemical) asymmetry must be externally engineered to create persistent chemical gradients that drive continuous self-propulsion [7, 15, 35, 44, 50, 74, 101–104]. The fact that the asymmetry necessary for self-propulsion needs to be engineered during synthesis of the microswimmer in the form of a catalytic metal deposited over part of its surface makes the fabrication of Janus microswimmers complex and infrastructure dependent. These are relatively difficult to fabricate in large numbers with uniform and controllable surface properties. Hence, the behaviour of Janus microswimmers is often less reproducible and less reliable in complex environments [86]. These limitations of Janus microswimmers have motivated a growing interest in chemically isotropic autophoretic microswimmers [21].

Autophoretic microswimmers achieve self-propulsion through *spontaneous symmetry breaking* of a chemical species triggered by advective perturbations, without the need for any engineered chemical asymmetry [64]. On one hand, for isotropic, chemically reactive colloidal particles, such spontaneous symmetry breaking of a chemical species created by surface chemical reactions leads to a phoretic slip velocity, which triggers interfacial flow and hence self-propulsion [63, 67]. On the other hand, for solubilizing droplets in a supramicellar surfactant solution, the spontaneous symmetry breaking of the filled micelle concentration leads to interfacial surfactant (interfacial tension) gradient, which drives interfacial flow triggering self-propulsion of the droplets [4, 29, 39, 46, 57, 62, 65, 75, 87, 93, 95]. Both isotropic chemically reactive colloidal particles and active droplets are canonical examples of autophoretic microswimmers. It is important to note here that for autophoretic microswimmers, the absolute necessity of advection for the symmetry breaking of the chemical species couples the evolution of the chemical concentration and the flow fields around the microswimmer through the non-linear advection terms in the species conservation equation, besides the pertinent hydrodynamic boundary conditions. This non-linear interplay between chemical concentration field and hydrodynamics results in interesting emergent dynamics for autophoretic microswimmers in complex environment.

In unbounded domains, theoretical and experimental studies have shown that increasing advective transport relative to diffusive effects, typically quantified by the increasing Péclet number, can destabilize steady swimming of autophoretic microswimmers due to chemo-hydrodynamic interactions giving rise to unsteady and even chaotic trajectories [14, 17, 31, 36, 62, 68]. In geometric confinements or during interaction between microswimmers, chemo-hydrodynamic coupling is further accentuated resulting in trapping of a microswimmer in the flow field of another microswimmer or near obstacles [40, 41]. Chemo-hydrodynamic interactions can also result in emergent collective behaviour, including formation of swimming chains [47, 92]; dynamic clusters [93, 96], transient caging phenomena [30], rotating clusters and self-organized vortical structures [8, 32], and emergent active turbulence [100]. Such interesting emergent phenomena stems from the nonlinear interaction between fluid flow and chemical signals produced by the autophoretic microswimmers. However, at the same time, non-linearity of the interaction makes the prediction of such emergent dynamics through theoretical and numerical modeling extremely challenging.

The principal challenge in modeling autophoretic microswimmers lies in the fact that these models must resolve the coupled Stokes flow and solute advection–diffusion with moving boundaries, since surface concentration gradients directly generate the slip velocity that drives propulsion [1, 21]. For the case of a single autophoretic microswimmer near a wall, or for two-swimmer interactions, the full chemo-hydrodynamic coupling can be addressed in bi-spherical coordinates [13, 52] using a combination of analytical and numerical methods. However, given the apparent complexity of this modeling technique, it will be difficult to extend the framework to capture emergent collective behaviour of autophoretic microswimmers. To address the collective behaviour, often the microswimmers are idealized as point sources instead of being finite-sized [51] or where rapid chemical diffusion and viscous momentum transport are assumed [83]. Although the simplified models enable the implementation of efficient large-scale solvers [12], it comes at the cost of failing to capture emergent phenomena driven by nonlinear chemohydrodynamic coupling.

Moving-boundary problems in the Stokes regime are commonly solved using boundary integral methods (BIM) based on Green's functions. BIM is the standard tool in microhydrodynamics, and works very well for viscous flows around passive particles [78]. However, for autophoretic microswimmers, resolving the chemical field throughout the fluid is computationally costly and typically scales as $\mathcal{O}(N^2)$ with the number of particles. Consequently, fully coupled chemo-hydrodynamic BIM approaches are hard to scale to large swimmer populations or strongly nonlinear regimes. Other numerical approaches have also been developed to handle fluid flow and solute transport with moving boundaries. The embedded boundary or cut-cell method [77] locally adjusts a Cartesian grid around each particle, giving sharp boundary resolution while leaving the rest of the grid fixed [60, 82]. The overlapping mesh method (OMM) divides the domain into multiple body-fitted, overlapping subdomains and interpolates values at the interfaces, allowing each subdomain to move independently [10, 28, 61, 80]. Although both approaches provide accurate boundary resolution, they are often complex to implement and are computationally expensive for many interacting particles, as grids must be reconstructed or interpolated at each timestep. To overcome these challenges, simpler fixed-grid approaches like the immersed boundary method [11, 98, 100] are often preferred. Here boundary forces as represented as source terms smoothly spread over nearby points, which avoids explicit boundary tracking and allows stable simulations of many particles. While this approach improves numerical stability, the diffuse interface limits the accurate enforcement of surface flux and slip conditions. Alongside these grid-based methods, particle-based frameworks such as multiparticle collision dynamics [70, 71], dissipative particle dynamics ([18, 33, 99]) and smoothed particle hydrodynamics ([34, 66, 89]) provide meshfree formulations that naturally capture mesoscale flows and complex interface physics. The recent numerical framework by [22] achieves high accuracy by explicitly resolving sharp moving boundaries through an overlapping mesh method for solute transport and a boundary-integral formulation for Stokes flow. However, this accuracy comes at the expense of increased computational complexity. Moreover, the chemo-hydrodynamic coupling is resolved through an iterative preconditioned procedure, whose convergence depends sensitively on relaxation parameters and typically requires multiple inner iterations per timestep.

In this work, we introduce an elegant, yet simplified, numerical framework for autophoretic microswimmers in which the fluid flow, solute transport, and particle motion are solved self-consistently on a single fixed grid. The incompressible Navier–Stokes equations are solved using a pseudospectral FFT-based solver with $N \log N$ scaling, while the solute concentration evolves according to the advection–diffusion equation on the same Eulerian grid. At each timestep, the swimmer's chemical activity is modeled by a smoothly distributed source centered at the particle, allowing the solute field to be evolved on a fixed grid without imposing surface flux boundary conditions. The resulting concentration gradient is computed on the grid and interpolated to the particle surface to evaluate the phoretic slip velocity [1, 21]. The resulting swimming velocity and swimming orientation then emerge naturally via the Lorentz reciprocal theorem [63], ensuring a fully self-consistent coupling between the chemical and hydrodynamic fields. Each particle is represented as a point stresslet whose strength depends on its instantaneous swimming velocity [48], which is regularized and spread onto the fluid grid as a forcing term [24], allowing its hydrodynamic influence to be incorporated globally without explicitly resolving particle boundaries. The updated flow subsequently advects the solute field, and the coupled system is advanced explicitly in time without the need for inner convergence iterations or moving meshes. Importantly, neither the particle velocity nor its orientation is prescribed; starting from a minimal initial perturbation that breaks the isotropic symmetry of the concentration field, both the magnitude and direction of propulsion arise autonomously from the evolving solute gradients. To estimate the efficacy of the proposed framework, we compare the numerically simulated dynamics of the autophoretic microswimmer with the swimming dynamics of autophoretic active droplets observed in independent experiments performed by us. Furthermore, we also test to what extent this new framework can capture the underlying chemo-hydrodynamic interactions that lead to some established complex motility patterns for autophoretic microswimmers, such as emergent destabilized swimming with increasing viscosity of the swimming medium ([31]) and pair-wise interactions mediated by chemotactic avoidance ([30]). To this end, we also compare the predictions from the numerical simulations with independently performed experimental results.

The paper has been organised as follows– § II describes the numerical simulations, § III outlines the experimental methodology, § IV presents and discusses the results, and § V provides the concluding remarks.

II. NUMERICAL SIMULATIONS

Model framework

We consider a chemically active circular disk of radius a, immersed in a Newtonian fluid of kinematic viscosity η, representing a two-dimensional analogue of an active droplet. Although we solve the full Navier–Stokes equations, the dynamics of such microswimmers are dominated by viscous forces, operating within the Stokesian regime (§II A). The concentration of the solute (filled micelles) is initialized uniformly throughout the domain, with small random perturbations to induce spontaneous symmetry breaking. The microswimmer continuously emits the solute isotropically, mimicking the filled micelles formation around an active droplet, but this isotropic state becomes unstable in the presence of perturbations, leading to an asymmetric solute distribution and tangential concentration gradients along the surface. This generates a slip velocity proportional to the surface concentration gradient resulting in self-propulsion while the swimmer remains force-free and torque-free (§II C–II B). The microswimmer's motion perturbs the surrounding fluid, which in turn redistributes the solute, thereby coupling solute transport to the hydrodynamic interactions (§II D). Thus, the microswimmer motion, the solute field, and the fluid flow are determined self-consistently through their mutual coupling, as described in the following subsections.

A. Fluid flow and vorticity formulation

To model quasi-two-dimensional flow, we solve the 2D incompressible Navier–Stokes equations in vorticity–streamfunction form:

$$\partial_t \omega + \mathbf{u} \cdot \nabla \omega = \nu \nabla^2 \omega + f_\omega^a, \tag{1}$$

$$\nabla^2 \psi = -\omega, \tag{2}$$

where $\mathbf{u}(\mathbf{x}, t) = \nabla^\perp \psi = (-\partial_y \psi, \partial_x \psi)$ is the velocity field. Here, $\omega = (\nabla \times \mathbf{u}) \cdot \hat{\mathbf{z}}$ is the vorticity and $\hat{\mathbf{z}}$ is the unit vector normal to the fluid film. The term f_ω^a accounts for perturbations to the surrounding fluid due to the microswimmer's motion (see § II D for details).
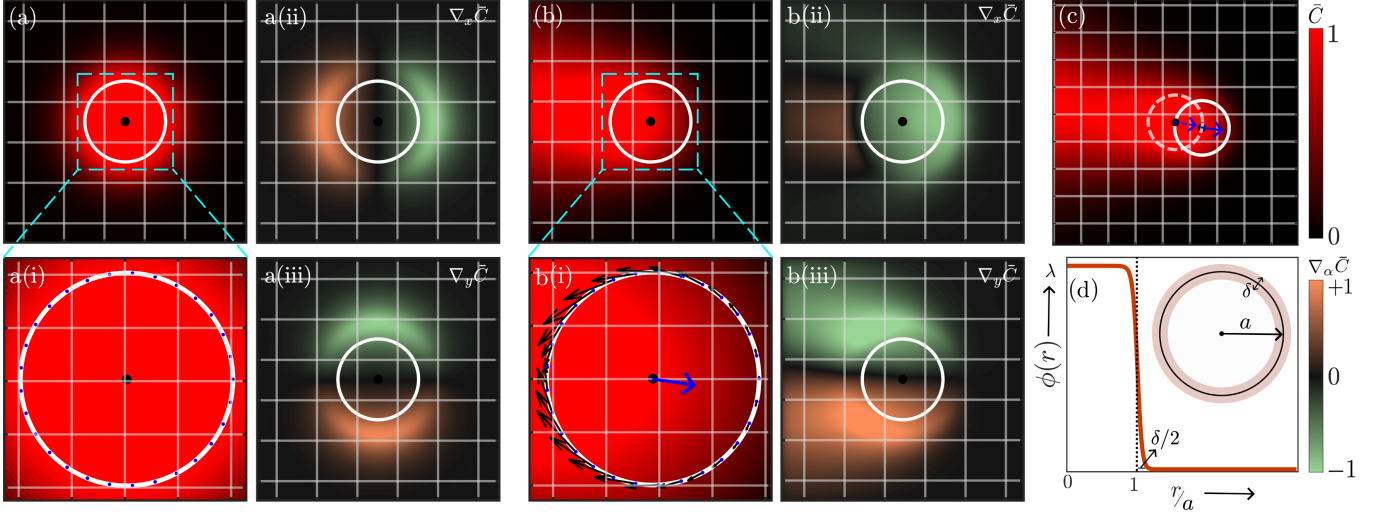
FIG. 1. **Schematic of the autophoretic microswimmer model.** (a) At low Péclet number (Pe), diffusion dominates, producing an isotropic solute field with uniform gradients throughout the domain. The Cartesian components of the concentration field shown in panels a(ii)–a(iii) remain perfectly symmetric, and the slip obtained from the discretised surface of the microswimmer in a(i) exhibits no tangential variation, resulting in zero propulsion. (b) At higher , advection becomes significant and the solute distribution develops weak anisotropy. Panels b(ii)–b(iii) show the resulting asymmetric concentration gradients, while b(i) illustrates the corresponding surface slip, which now has a finite mean component and drives motion opposite to the region of strongest slip. (c) A zoomed-out view highlights the swimmer's displacement relative to its self-generated concentration field. (d) Radial solute distribution $\phi(r)$ (red curve) around a microswimmer, modeled using a hyperbolic-tangent profile with surface concentration λ, particle radius a , and decay length δ that sets the distance over which the concentration relaxes to the background value. The inset schematic shows the microswimmer of radius a and the surrounding decay layer (beige annulus of thickness δ).

B.   Solute emission and concentration field evolution

Each microswimmer of radius 'a' acts as a localized chemical source, continuously emitting solute into the surrounding fluid, whose concentration field subsequently evolves through the combined effects of swimmer activity, advection by the flow, and molecular diffusion.

At the start of the simulation, the solute concentration is initialized as a uniform background field with a small random perturbation,

$$C(\boldsymbol{r}, t_0) = C_0 + \xi(\boldsymbol{r}), \tag{3}$$

where C_0 is a constant reference concentration and $\xi(\boldsymbol{r})$ is an uncorrelated, low-amplitude noise field introduced to seed spontaneous symmetry breaking. In the absence of any flow, diffusion rapidly smooths out these perturbations.

Chemical activity is implemented by placing a localized solute source at the instantaneous center of the microswimmer $\mathbf{r}_i(t)$. The microswimmer emits solute at a prescribed rate λ, with a spatial distribution modeled by a smooth hyperbolic-tangent profile (Fig. 1(d)),

$$\phi(\mathbf{r}) = \frac{\lambda}{2} \left[1 - \tanh\left(\frac{|\mathbf{r} - \mathbf{r}_i| - a}{\delta} \right) \right]. \tag{4}$$

where δ controls the thickness of the solute boundary layer surrounding the swimmer. This regularization avoids discontinuities at the particle surface while preserving a well-defined source region of size a.

The time evolution of the solute concentration is governed by an advection–reaction–diffusion equation,

$$\partial_t C + \mathbf{u} \cdot \nabla C = D \nabla^2 C + \phi(\boldsymbol{r}), \tag{5}$$

where D is the solute diffusivity and $\mathbf{u}$ is the fluid velocity field obtained from §II A. At each time step, newly emitted solute is added to the concentration field via the source term ϕ.

The interplay of activity, advection, and diffusion generates strong concentration gradients in the immediate vicinity of the swimmer, while farther from the particle the solute distribution relaxes smoothly toward the background concentration. As shown in Fig. 1(a), diffusion dominates at low Péclet number (Pe) (see § IV for the definition of

Pe), leading to an essentially isotropic concentration field. At higher Péclet number (Fig. 1(b)), advection distorts the solute distribution and produces anisotropic gradients along the swimmer surface, which drive phoretic slip and self-propulsion (Fig. 1(c)) (§II C).

C. Phoretic slip and self-propulsion

Gradients in the solute concentration along a microswimmer's surface generate a local phoretic slip velocity ([1, 64])

$$\mathbf{u}_s = M\nabla_\| C, \tag{6}$$

where M is the phoretic mobility, $\nabla_\|$ is the surface gradient, and C is the solute concentration evaluated at the microswimmer boundary. For an isotropic concentration field, the surface-averaged slip vanishes and the swimmer remains stationary.

The instantaneous swimming velocity of a force-free microswimmer follows from the Lorentz reciprocal theorem [85] and is determined solely by the surface slip velocity. In two dimensions, this relation reduces to a line integral along the particle boundary ∂B,

$$\mathbf{u}_0 = -\frac{1}{2\pi a}\int_{\partial B}\mathbf{u}_s\, dl = -\frac{M}{2\pi a}\int_{\partial B}\nabla_\| C\, dl. \tag{7}$$

The negative sign indicates that the swimmer moves opposite to the surface slip, corresponding to an anti-chemotactic response for $M > 0$.

At low Pe, diffusion suppresses concentration anisotropies, resulting in nearly uniform surface gradients and vanishing propulsion (Fig. 1(a)). As the Pe increases, advection distorts the solute field and generates anisotropic surface gradients, leading to a finite mean slip and sustained self-propulsion (Fig. 1(b)).

To evaluate the surface integrals numerically, the circular swimmer boundary is discretized into n uniformly spaced points. At each point, the surface concentration gradient is obtained by interpolating the grid-based solute field, and the swimming velocity is approximated as

$$\mathbf{u}_0 \approx -\frac{M}{n}\sum_{k=1}^{n}(\nabla_\| C)_k \tag{8}$$

where $(\nabla_\| C)_k$ is the surface gradient at the k-th boundary point.

Once a finite swimming velocity is established, the instantaneous position of the microswimmer center $\boldsymbol{r}_i$ is updated according to

$$\partial_t \boldsymbol{r}_i = \boldsymbol{v}_d \tag{9}$$

where the total velocity $\boldsymbol{v}_d$ of the micromicroswimmer is

$$\boldsymbol{v}_d = \mathbf{u}_0 + \mathbf{u}(\boldsymbol{r}_i) + \sum_{i\neq j}\mathbf{F}_{ij} \tag{10}$$

Here, $\mathbf{u}(\boldsymbol{r}_i)$ represents advection by the ambient fluid at the centre of the micromicroswimmer, and $\mathbf{F}_{ij}$ accounts for steric interactions with neighboring microswimmers.

Steric repulsion is modeled as a short-ranged, linearly decaying force,

$$\boldsymbol{F}_{ij} = \begin{cases} F_0\left(1 - \dfrac{r_{ij}}{2a}\right)\mathbf{e}_{ij}, & r_{ij} < 2a, \\ 0, & \text{otherwise,} \end{cases} \tag{11}$$

where F_0 is the repulsion strength, $r_{ij} = |\boldsymbol{r}_j - \boldsymbol{r}_i|$ is the distance between the microswimmer centers, and $\mathbf{e}_{ij} = (\boldsymbol{r}_j - \boldsymbol{r}_i)/r_{ij}$ is the unit vector pointing from microswimmer i to j. For an isolated swimmer in the absence of ambient flow, $\boldsymbol{v}_d = \mathbf{u}_0$.

D. Hydrodynamic signature and stresslet modeling

The self-propulsion of a microswimmer not only drives its own motion but also disturbs the surrounding fluid over long distances. Microswimmers swim without exerting a net force or torque on the fluid, and as a result the leading-order far-field flow has the symmetry of a force dipole, known as a stresslet [3, 38]. This stresslet can be calculated directly from the surface slip velocity using the reciprocal theorem, without solving for the full flow field [48]. Following this approach, we have modeled each swimmer in our simulations as a point stresslet centered at its instantaneous position $\mathbf{r}_i$, with strength

$$\sigma_0 \propto \alpha a^2 \nu u_0(t),$$

where $\alpha > 0$ for pullers and $\alpha < 0$ for pushers. Since a point stresslet corresponds to a delta-function stress distribution, we distribute it smoothly into the surrounding fluid using a Gaussian kernel [24, 53–55, 59]. This regularization ensures smooth coupling between the swimmer and the fluid, improves numerical stability, and preserves the essential character of the stresslet while remaining computationally efficient.

The resulting regularized stress field is written as

$$\mathbf{S}(\mathbf{r}, t) = \sum_{i=1}^{N_p} \frac{\sigma_0}{(2\pi\epsilon^2)^{3/2}} \left(\hat{\mathbf{e}}_i \hat{\mathbf{e}}_i - \tfrac{1}{2}\mathbf{I}\right) \exp\left[-\frac{|\mathbf{r}-\mathbf{r}_i|^2}{2\epsilon^2}\right], \tag{12}$$

where $\hat{\mathbf{e}}_i$ (Fig. 2(b),inset) is the swimmer orientation and ϵ the Gaussian width, effectively representing the size of the swimmer. N_p is the total number of microswimmers. Although a swimmer does not act directly on itself through this stress, the flow field generated by the regularized stress advects the surrounding solute, thereby coupling the chemical and hydrodynamic fields. In the simulations, the active forcing that drives the fluid motion is obtained from the divergence of the regularized stress field,

$$\mathbf{f}^a = \nabla \cdot \mathbf{S}, \tag{13}$$

which, in the streamfunction–vorticity formulation, enters as

$$f_\omega^a = \nabla \times (\nabla \cdot \mathbf{S}). \tag{14}$$

This formulation enables a self-consistent coupling between swimmer activity, hydrodynamic interactions, and solute transport while remaining computationally tractable for large-scale simulations.

E. Numerical methodology

We perform direct numerical simulations (DNSs) of Eqs. (1)–(5) in a doubly periodic square domain $[0, 8\pi]^2$ using a pseudo-spectral method [9, 25]. We represent the flow and concentration fields on a uniform 1024^2 grid. We compute spatial derivatives in Fourier space and evaluate nonlinear terms in physical space via transform–multiply–inverse-transform. We remove aliasing using the two-thirds truncation [72], and FFTW provides fast transforms [19]. Grid-refinement tests at $N = 512, 1024, 2048$ show negligible changes in statistics and swimmer velocities, so we adopt $N = 1024$.

We solve the two-dimensional incompressible Navier–Stokes equations using a vorticity–streamfunction formulation [25, 73, 76], with $\mathbf{u} = (\partial_y\psi, -\partial_x\psi)$ ensuring incompressibility. We advance time using a second-order exponential time-differencing Runge–Kutta (ETD-RK2) [79], which treats diffusive terms exactly and nonlinear terms explicitly. We use a fixed step $\Delta t = 10^{-3}$ that satisfies the Courant–Friedrichs–Lewy (CFL) condition $\max|\mathbf{u}|\Delta t/\Delta x \lesssim 1$, where $\Delta x = 8\pi/N$.

We vary the viscosity over $\nu \in [8 \times 10^{-3}, 5]$ and prescribe the diffusivity as $D = D_0/\nu$ ($D_0 = 8 \times 10^{-3}$), which tunes the (Pe) number without destabilising the solver. The advection–diffusion implementation matches the four-roll mill benchmark [84, 91].

We obtain concentration gradients at the swimmer surface by bilinear interpolation from the Eulerian concentration gradient field to Lagrangian boundary points [25]. We introduce swimmer forcing as a regularised body-force density with Gaussian width $\epsilon = a/(6\sqrt{\pi})^{1/3}$ (§. II D), which provides smooth coupling on the grid. The solute activity layer (Eq. (4)) has thickness $\delta \simeq 5\Delta x$, which is resolved at the chosen grid spacing.

The governing equations are solved in dimensional form. This preserves the direct physical meaning of parameters and simplifies coupling between solute transport, hydrodynamics, and swimmer activity when multiple length and

time scales coexist. Dimensionless groups such as the Reynolds and Pe numbers are evaluated a posteriori to classify regimes.

We impose swimmer forcing as a body force rather than a boundary condition, which avoids explicit surface meshing and remains compatible with the spectral solver and periodic geometry, while reproducing the correct far-field stresslet structure [24, 54, 55].

III. EXPERIMENTAL METHODOLOGY

A. Fabrication of quasi-2D reservoir

The reservoir is fabricated using standard photolithography and softlithography processes with dimensions of 5×5 mm^2 and a height of 50μm. The height of the reservoir is designed to be $\sim 2a$ in order to confine the micromicroswimmers, i.e. active droplets, to swim in the horizontal $X - Y$ plane, effectively resulting in a quasi-two-dimensional (quasi-2D) reservoir. We use polydimethylsiloxane (PDMS) (SYLGARD 184, Dow Chemicals) mixed in the base polymer to the crosslinker ratio of $10 : 1$. We pour the PDMS prepolymer onto the reservoir mold, and cure it in a hot air oven for 3 hours at 75 °C. Similarly, we coat a cover-slip (160 μm in thickness, Corning) with the same pre-polymer film and cure it for 3 hours at 75 °C. Upon curing, we peel off the cured PDMS stamp, having the negative replica of the mold, and create the inlet and outlet reservoirs using sharp punctures. We then bond the PDMS stamp to a glass slide coated with a PDMS film using a plasma oxidation process.

B. Generation of active droplets

We generate the active (self propelling) oil droplets using a microfluidic flow focusing device ([23]). In the microfluidic flow focusing device, the two streams of 0.1 wt% aqueous surfactant (Trimethyl(tetradecyl)ammonium bromide, TTAB ; Sigma-Aldrich) solution pinch off the CB-15 liquid crystal oil (PureSynth) stream creating droplets of $2a \approx 43.34 \pm 1.88$ μm in diameter. We generate and store the CB15 oil droplets in 0.1 wt% aqueous TTAB solution which is lower than the critical miceller concentration for TTAB (CMC=0.13 wt%). During the experiments, we mix these oil droplets with 7.5 wt% aqueous TTAB solution to make them active and subsequently introduce them into the reservoir.

C. Bright field and fluorescence microscopy

The trajectories of the active droplet are visualized using bright-field imaging using an inverted Nikon ECLIPSE Ti microscope. We track the active droplet using a CMOS monochrome digital camera integrated with the microscope (IDS Imaging), having an image resolution of 1920×1200 pixels. We record the image sequence at 25 frames per second, with a 20X objective having a spatial resolution of 0.2802 μm/pixel The centroid of the active droplet is evaluated using an in-house MATLAB post-processing code. The instantaneous velocity of the active droplet is calculated using the central difference method as $v_{d_x}(t) = (x(t + \Delta t) - x(t - \Delta t))/2\Delta t$ and similarly for v_{d_y}. Using v_{d_x} and v_{d_y} we calculate the instantaneous angular orientation as $\psi = \tan^{-1}(v_{d_y}/v_{d_x})$.

We visualize the flow field generated by the active droplet using a high-resolution micro Particle Image Velocimetry (μPIV) technique. The continuous medium (7.5 wt% aqueous TTAB solution) is seeded with the fluorescent tracer particles of 500 nm size (carboxylate-modified, Thermo Fisher Scientific) having excitation/emission wavelengths of 505/515 nm. The tracer particles are mixed in a ratio of $1 : 20$ by volume in the aqueous TTAB solution, and we sonicate the mixture to prevent coagulation of the tracer particles. We then add the generated CB15 oil droplets in this solution (7.5 wt% aqueous TTAB solution + tracer particles) in a ratio of $1 : 5$ by volume to make them active. To visualize and quantify the flow field generated by the active droplets, the tracer particles are excited using a 100 W mercury lamp (Nikon, Model: LH-M100C-1) attached to the inverted Nikon ECLIPSE Ti microscope. The required excitation wavelength is passed through a filter cube having the two peak excitation wavelengths of 487/562 nm and emission wavelengths of 523/630 nm (Chroma Technology, Model: 59009 - ET - FITC/CY3). We record the image sequence at 25fps and post-process the image sequence in an open source platform integrated with MATLAB 2024a ([90]).

D. Evaluation of chemical (filled micelle) kymographs

To visualize the chemical wake generated by the active droplets, we tag the CB15 oil with fluorescent Nile Red dye (Invitrogen™; excitation/emission: 550/640 nm) and generate the droplets using the microfluidic flow focusing device and store them in an aqueous surfactant solution having the surfactant concentration lower than the CMC level (0.1 wt%). As explained in the previous section, we make the droplets active by mixing them in the 7.5 wt% aqueous TTAB solution and introduce them into the quasi-2D reservoir. During the solubilization process of the active droplets, the empty micelles get converted to filled micelles containing the CB15 oil, which contains the fluorescent Nile red dye. This chemical wake generated by the active droplet as it self-propels is visualized using the inverted microscopy equipped with a dual-band filter (Chroma Technology, Model : 59009 - ET - FITC/CY3). The image sequence is captured at 25 frames per second, and the exposure is set so that the image does not oversaturate (Fig. 3(d)).

The image sequence is post-processed using an in-house Matlab 2024a code. We extract the pixel intensities $I(\theta)$ in a CCW direction ($\theta \in [0, 2\pi]$) at a distance of $22\mu m$ from the active droplet circumference. The kymograph is generated by plotting the temporal variation of $I(\theta)$ around the active droplet over time (Fig. 3(e)). Additionally, the diffusion profile of the filled micelles over time, originating from the chemical trail left behind as the active droplet swims away, is analyzed by extracting the pixel intensities (I) along a fixed line perpendicular to the posterior apex of the active droplet (Fig. 3(f)).

E. Variation of the viscosity of the swimming medium

The viscosity of the continuous medium (7.5 wt% aqueous TTAB solution) is varied by mixing glycerol (99%; Sigma-Aldrich) at concentrations of 40% and 60% by volume in the total solution. We characterize the viscosity of the continuous medium mixed with glycerol and surfactant using the Anton Paar rheometer rotational rheometer (RheolabQC). The dynamic viscosities of 40% and 60% glycerol by volume are measured in the shear rate range of $10 < \dot{\gamma} < 1500$ s^{-1}, and are calculated to be 3.5 mPas and 11.5 mPas, respectively.

IV. RESULTS AND DISCUSSIONS

For effective comparison between simulations and experiments, we non-dimensionalize both the simulation and experimental results using the appropriate scales– spatial variables by the microswimmer radius a (simulation, $a = 1$; experiments, $a = 21.67 \pm 0.94$ μm); velocity magnitude (v_d) by the average swimming speed ($\langle v_d \rangle$)with the least fluctuation in a low viscosity swimming medium (simulation, $U_0 \sim 0.58$; experiments, $U_0 = 17.7886 \pm 2.07$ μm/s is the average swimming speed in the aqueous TTAB solution); and time by the advective time scale $t_0 = a/U_0$. Based on such non-dimensionalization scheme, the Péclet number (Pe) for the model microswimmer system can be defined as Pe $\approx U_0 a/D(\nu)$, where $D(\nu)$ is the viscosity-dependent diffusion co-efficient of the chemical emitted by the microswimmer. The simulation exhibits symmetry-breaking of the chemical concentration over the microswimmer length scale, and the onset of self-propulsion, at a critical Pe ≈ 1. This is relatively smaller than the critical Pe ≈ 4 for the experimental system considering the pure aqueous TTAB solution as swimming medium. But, importantly, the numerical prediction of Pe $\approx 1 \sim \mathcal{O}(1)$ at the onset of self-propulsion is consistent with the theoretical requirement for self-propulsion of isotropic, autophoretic microswimmers due to spontaneous symmetry breaking [64].

A. Predictions for swimming characteristics and hydrodynamic signature at low Pe

In simulations for Pe ≈ 4, the microswimmer swims along a persistent trajectory with steady speed ($\bar{v}_d$) (Fig. 2(a)), and without alterations in the swimming orientation ψ (Fig. 2(b)); also see video S1 for Pe ≈ 6, which exhibits dynamics equivalent to those observed at Pe ≈ 4). Here, ψ is the orientation of the instantaneous swimming velocity vector $\boldsymbol{v_d} = v_d \hat{\boldsymbol{e}} = v_d(\cos \psi \ \hat{\boldsymbol{i}} + \sin \psi \ \hat{\boldsymbol{j}})$ (inset in Fig. 2(b)). These swimming characteristics are consistent with the steady, unidirectional swimming exhibited by a model autophoretic microswimmer, such as an active droplet, in experiments for low Pe ≈ 4 (Figs. 2(d) and (e)). Furthermore, we perform a quantitative comparison between the numerically simulated and experimentally observed swimming dynamics at low Pe using the mean–squared displacement (MSD) (Fig. 2(g)) and the angular autocorrelation function C_{vv} (Fig. 2(h)). The MSD is computed as

$$\langle \Delta r^2(\Delta t) \rangle = \left\langle \left[\boldsymbol{r}(t_0 + \Delta t) - \boldsymbol{r}(t_0) \right]^2 \right\rangle_{t_0}, \tag{15}$$
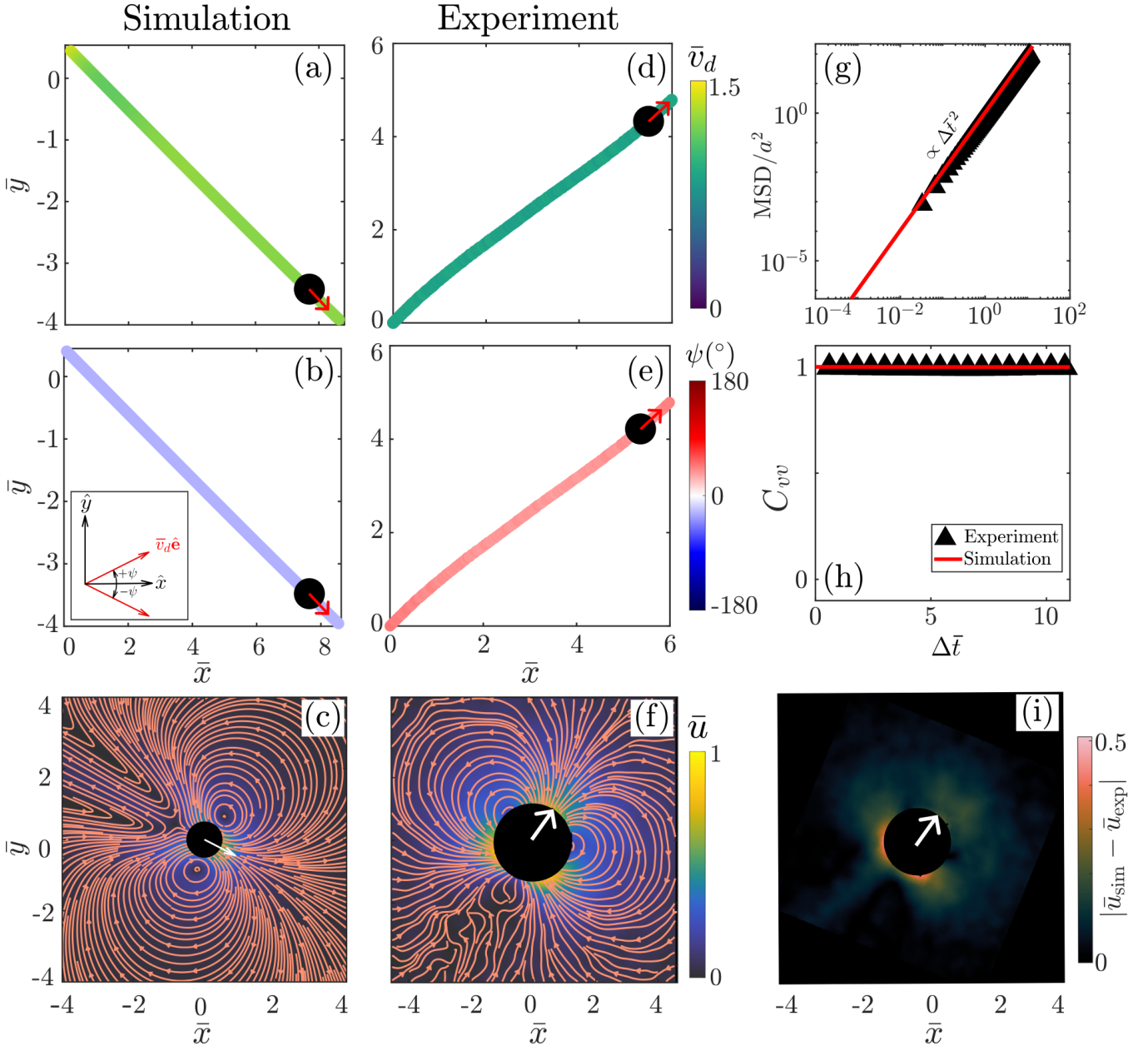
FIG. 2. **Comparison between simulation and experimental results for microswimmer dynamics and hydrodynamic signature at low** Pe **number.** *First column (Simulation):* Trajectory of the microswimmer (a) color-coded with the non-dimensional swimming speed $\bar{v}_d$, and (b) colour-coded with the swimming orientation as given by the orientation angle ψ of the swimming velocity vector (inset). (c) The flow field generated by the microswimmer represented using streamlines and contour plot for the local velocity magnitude $\bar{u}$. The results shown here are for simulations at Pe ≈ 4. *Second column (Experiment):* (d)-(f) Corresponding experimental observations for Pe $= 4$. Temporal variations of the (g) mean-squared displacement (MSD) and (h) angular autocorrelation function (C_{vv}) for the swimming trajectory as obtained from the simulations (red line) and experiments (symbols). (i) The contour plot of the magnitude of the difference between simulation and experimental values of the local flow speed around the microswimmer swimming along identical direction.

where the average is taken over all reference times t_0 and particle trajectories. The MSD for both the simulations (solid line) and the experiments (symbols) exhibit ballistic scaling $\langle \Delta r^2(t) \rangle \propto \Delta t^2$ (Figs. 2(g)), which is commensurate with the persistent propulsion over time observed in both the cases. The angular autocorrelation function is defined as

$$C_{vv}(\Delta t) = \left\langle \frac{\boldsymbol{v}_d(t_0 + \Delta t) \cdot \boldsymbol{v}_d(t_0)}{|\boldsymbol{v}_d(t_0 + \Delta t)| \, |\boldsymbol{v}_d(t_0)|} \right\rangle_{t_0}, \tag{16}$$
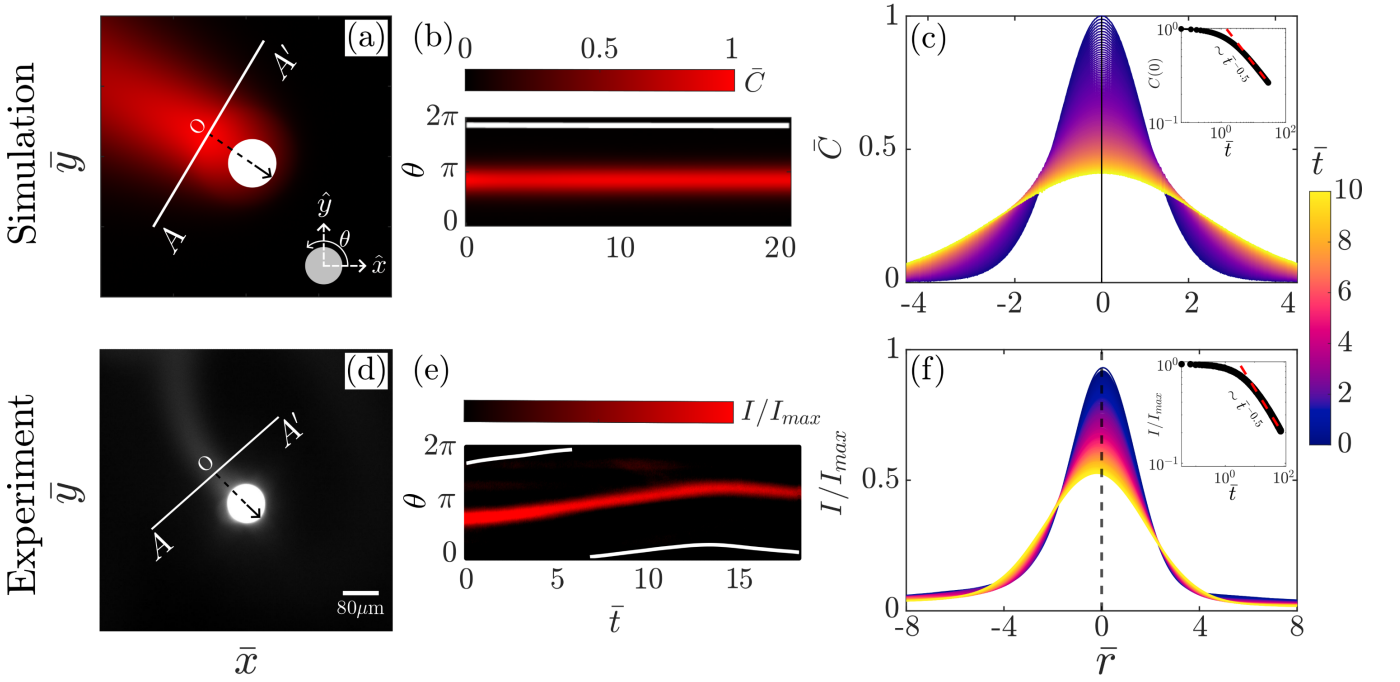
FIG. 3. **Comparison between simulation and experimental results for the spatio-temporal evolution of the chemical trail ejected by the autophoretic microswimmer at low** Pe $\approx$ 4**.** *Top row (Simulation):* (a) A simulation snapshot showing the self-generated chemical trail left behind by the microswimmer during its self-propulsion. (b) Kymograph depicting the temporal evolution of the chemical concentration ($\bar{C}$) around the microswimmer's circumference, with angular position θ measured counterclockwise from the $+x$-axis (inset in a). The white line shows the swimming orientation in terms of θ. (c) Temporal evolution of the chemical concentration along a fixed straight line AA′ (shown in a), drawn perpendicular to the instantaneous swimming orientation and passing through the microswimmer's center of mass. Inset: log–log plot showing a $\propto t^{-1/2}$ decay of the chemical concentration at a fixed point O on AA′. *Bottom row (Experiment):* (d) Fluorescence micrograph showing the chemical (filled micelle) trail left behind by the active droplet. (e) Corresponding kymograph of fluorescence intensity $I(\theta)$ (filled micelle concentration) around the active droplet periphery during its self-propulsion. (f) Evolution of the filled micelle concentration along a fixed line AA′ as in (d). The inset also shows the $\propto t^{-1/2}$ decay of the filled micelle concentration.

Here also, C_{vv} is averaged over all reference times t_0 and trajectories. The auto-correlation function C_{vv} computed from both simulation and experimental data remains constant about 1 (Fig. 2(h)), as expected for the unidirectional swimming.

The numerical model predicts a dipolar flow field generated by the autophoretic microswimmer (Fig. 2(c)) during self-propulsion at low Pe, as is also seen in the experiments with the active droplet (Fig. 2(f)). To further pin-point the quantitative accuracy of the numerical prediction for the hydrodynamic signature, we show in Fig. 2(i) the contour plot for the magnitude of the difference (residual) between the local values of the flow speed around a microswimmer, oriented in an identical manner, obtained from the simulations and experiments. The numerically estimated flow field (Fig. 2(c)) is closely aligned with the theoretical prediction for a spherical, autophoretic microswimmer at low Pe, in which case the flow field is dominated by the first hydrodynamic mode i.e. essentially a source dipole [31, 64]

B. Spatio-temporal evolution of the chemical trail emitted by the microswimmer

The proposed numerical simulation strategy captures the evolution of the chemical (exhaust) trail generated by the autophoretic microswimmer (Fig. 3(a); also see video S1). This is analogous to the chemical (oil-filled micelle) trail left behind by the active droplet as observed in the experiments (Fig. 3(d)). The kymograph constructed from the simulation results (Fig. 3(b)) shows the temporal evolution of the distribution of chemical concentration ($\bar{C}$) around the microswimmer's periphery during its self-propulsion. Here, θ is measured counterclockwise from $+\hat{x}$ (inset in Fig. 3(a)). At low Pe($\approx$ 4), since the microswimmer swims steadily, the chemical wake remains uniform in thickness over the swimming trajectory and fixed about the posterior apex i.e. diametrically opposite to the instantaneous swimming orientation (white line in Fig. 3(b)). Note that the emergent circumferential non-uniformity of the chemical

concentration sustains the surface slip velocity necessary for self-propulsion, and agrees with theoretical predictions for autophoretic microswimmers with uniform surface activity [63]. The experimentally obtained kymograph (Fig. 3(e)) shows a similar angular distribution of the filled micelle concentration, with the maximum concentration consistently located at the posterior apex of the active droplet (i.e. diametrically opposite to the local swimming orientation given by the white line).

We also track the spatio-temporal evolution of the chemical trail in the swimming medium away from the microswimmer. To this end, we evaluate the evolution of $\bar{C}$ along a fixed line AA' passing through the self-generated trail and orthogonal to the local swimming orientation (Fig. 3(a)). The evolution of $\bar{C}$ along AA' follows a one-dimensional Gaussian distribution (Fig. 3(c)):

$$C(r,t) \sim \frac{1}{\sqrt{4\pi D(\nu)t}} \exp\left(-\frac{r^2}{4D(\nu)t}\right), \tag{17}$$

where r is the distance from the center of the trail along AA'. Furthermore, the inset in Fig. 3(c) shows that the peak concentration along AA' follows $\propto t^{-1/2}$ decay. Therefore, the evolution of the self-generated chemical trail in the swimming medium is diffusive in nature. This is commensurate with the results from the experimentally observed evolution of the filled micelle trail left behind by the active droplet (Fig. 3(f)). Note then that the time scale for the diffusion-driven evolution of the chemical trail in the swimming medium is $t_{diff} \sim a^2/D(\nu) \sim 8$, while the advective time scale for the propulsion of the microswimmer is $t_{adv} \sim a/U_0 \sim 2$. Since $t_{diff} > t_{adv}$, in our simulations, the medium is capable of retaining a memory of the microswimmer's trajectory as has been argued for physical, autophoretic systems [30].

The agreement between numerical simulation and experimental results across microswimmer trajectories, flow fields, statistical measures, and the evolution of the self-generated chemical trail highlights the fact that the proposed numerical framework accurately captures the swimming dynamics of an autophoretic microswimmer, such as an active droplet. The aforementioned discussions establish the foundation for investigating the efficacy of the proposed model in predicting more complex chemo-hydrodynamic interactions for autophoretic microswimmers.

C. Emergent complex motility at higher Péclet numbers

Autophoretic microswimmers, like active droplets, adapt to increasing viscosity of the swimming medium, culminating in increasing Pe, by spontaneously altering their motility from quasi-ballistic to chaotic (disordered) [14, 31]. We have performed experiments that recreate this transition in swimming motility of active droplets with increasing viscosity of the swimming medium achieved by adding increasing weight percentage of glycerol to the aqueous TTAB solution (Fig. 4(b)(i-iii)). Note that the increasing viscosity of the swimming medium results in gradual increase in Pe due to the gradual decrease in $D(\nu)$. Interestingly, the numerical simulation framework presented here predicts the emergence of such destabilized motion of an autophoretic microswimmer with increasing Pe (Fig. 4(a)(I-IV); also see video S2 and video S3 (in video S3 the trajectory color coded with velocity is stitched and shown in 16π domain for continuity and clarity as the microswimmer exits and re-enters the 8π domain of the simulation, while the concentration field is shown in 8π). For Pe ≤ 6, the microswimmer exhibits steady quasi-ballistic swimming as explained before (Fig. 4(a)(I)and (b)(i)). With increasing viscosity of the swimming medium, i.e., with increasing Pe beyond 6, the numerical trajectories show that the microswimmer exhibits exceedingly frequent reorientations in the swimming direction resulting in the loss of unidirectional swimming (Fig. 4(a)(II-IV)). Furthermore, the reorientations in the swimming direction are accompanied by changes in $\bar{v}_d$. Specifically, the local reorientation of the microswimmer is preceded and followed by its slowing down and speeding up respectively (Fig. 4(a)(II-IV)). These predictions closely mirror the experimental observations for increasing Pe (Fig. 4(b)(ii-iii)).

Statistical analyses of the numerical simulation results further substantiate the aforementioned observations made based on the trajectories. The average swimming speed increases until Pe ~ 6 while the associated standard deviation std_{v_d} decreases representing steady, quasi-ballistic swimming (Fig. 4(c)). For Pe > 6, the probability distribution $(P(\bar{v}_d))$ of $\bar{v}_d$ becomes progressively broader with increasing Pe (Fig. 4(d)) indicating the increasing fluctuations in propulsion speed over the trajectory. With increasing Pe, on the one hand, the increasing probability of events with low swimming speed represents the higher occurrence of the slowing down of the microswimmer prior to reorientation (Fig. 4(d)). On the other hand, the gradual emergence of the tail of the distribution represents the local acceleration of the microswimmer following the reorientation. As a consequence of such fluctuations in the propulsion speed, $\langle v_d \rangle$ gradually decays, while the associated standard deviation std_{v_d} increases, with increasing Pe (Fig. 4(c)). Such variation of $\langle v_d \rangle$ with Pe as shown in Fig. 4(c) is commensurate with the established theoretical results for autophoretic microswimmers in axisymmetric problems [39, 68, 69]. The apparent loss of ballistic swimming with increasing Pe is also captured by the mean-squared displacement (MSD) plots (Fig. 4(e)). With increasing Pe, the scaling for MSD
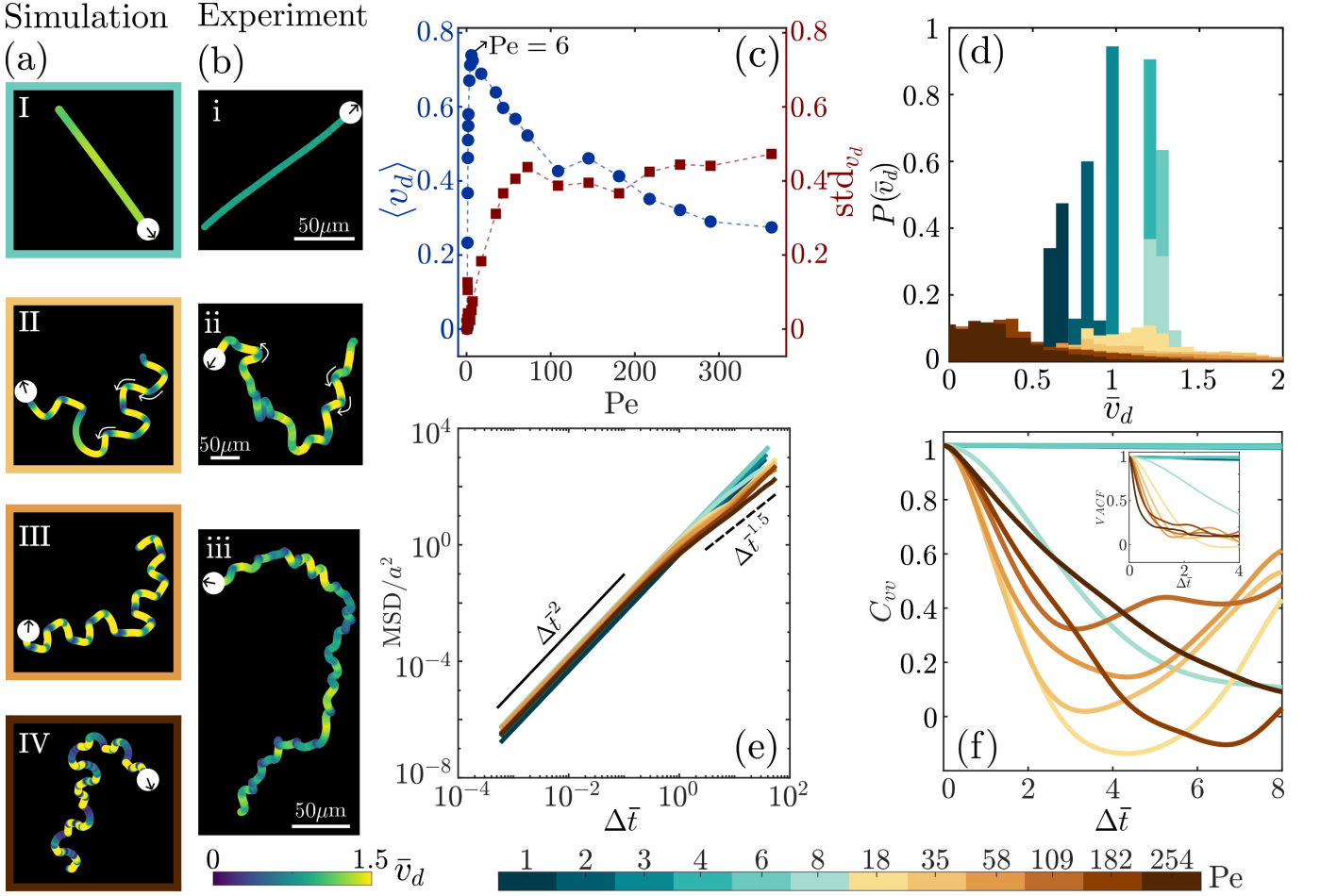
FIG. 4. **Emergent motility of the microswimmer with increasing viscosity of the swimming medium culminating in increasing Péclet number.** (a)(I-IV) Simulated microswimmer trajectories for increasing Pe $\in \{6, 35, 58, 254\}$ color-coded by the non-dimensional propulsion speed $\bar{v}_d$. (b)(i-iii) Experimental trajectories for increasing Pe $\in \{4, 15, 50\}$ corresponding to increasing viscosity of the swimming medium (achieved by adding increasing weight percentage of glycerol to aqueous TTAB solution- 0%, 40%, and 60%). The white circles representing the active droplet are not to scale. *Statistical analyses of numerical simulation results:* (c) Variations of the average swimming speed($< v_d >$) and its standard deviation (std_{v_d}) with increasing Pe. (d) Probability distributions of the non-dimensional, instantaneous propulsion speed ($\bar{v}_d$) for different Pe. (e) Variations of mean squared displacement (MSD), non-dimensionalized by a^2, with time interval Δt for increasing Pe. (f) Variations of the angular autocorrelation function (C_{vv}) with time interval Δt for increasing Pe. The inset shows the corresponding velocity autocorrelation function ($VACF$), highlighting a monotonic decay of velocity correlations with time interval Δt.

deviates from the ballistic ($\propto \Delta \bar{t}^2$) to the sub-ballistic ($\propto \Delta \bar{t}^{1.5}$) at long times ($\Delta \bar{t} \sim \mathcal{O}(1) - \mathcal{O}(10)$). Furthermore, the loss of unidirectional swimming with increasing Pe due to frequent reorientations of the microswimmer is evident from the corresponding variations of C_{vv} with time interval $\Delta \bar{t}$ (Fig. 4(f)). For Pe ≤ 6, C_{vv} remains constant about 1 indicating unidirectional swimming. However, for Pe > 6, C_{vv} decays with $\Delta \bar{t}$ highlighting the gradual decorrelation between the swimming orientations with time interval. Note that beyond Pe ~ 35, the decay in C_{vv} with $\Delta \bar{t}$ becomes relatively slower (Fig. 4(f)) indicating non-monotonic decay in $C_{vv}(\Delta \bar{t})$ with increasing Pe. The slower decay in C_{vv} at higher Pe stems from the fact that reorientations over shorter time intervals are weaker due to more frequent slowing down of the microswimmer including local stalling. However, the dimensional velocity autocorrelation function ($VACF(\Delta t) = \left\langle \frac{\boldsymbol{v_d}(t_0 + \Delta t) \cdot \boldsymbol{v_d}(t_0)}{|\boldsymbol{v_d}(t_0)|^2} \right\rangle_{t_0}$); inset Fig. 4(f)) shows a monotonic decay with increasing Pe because the magnitude of the swimming speed decorrelates even at small time intervals (i.e. faster) precisely due to such frequent slowing down of the microswimmer.
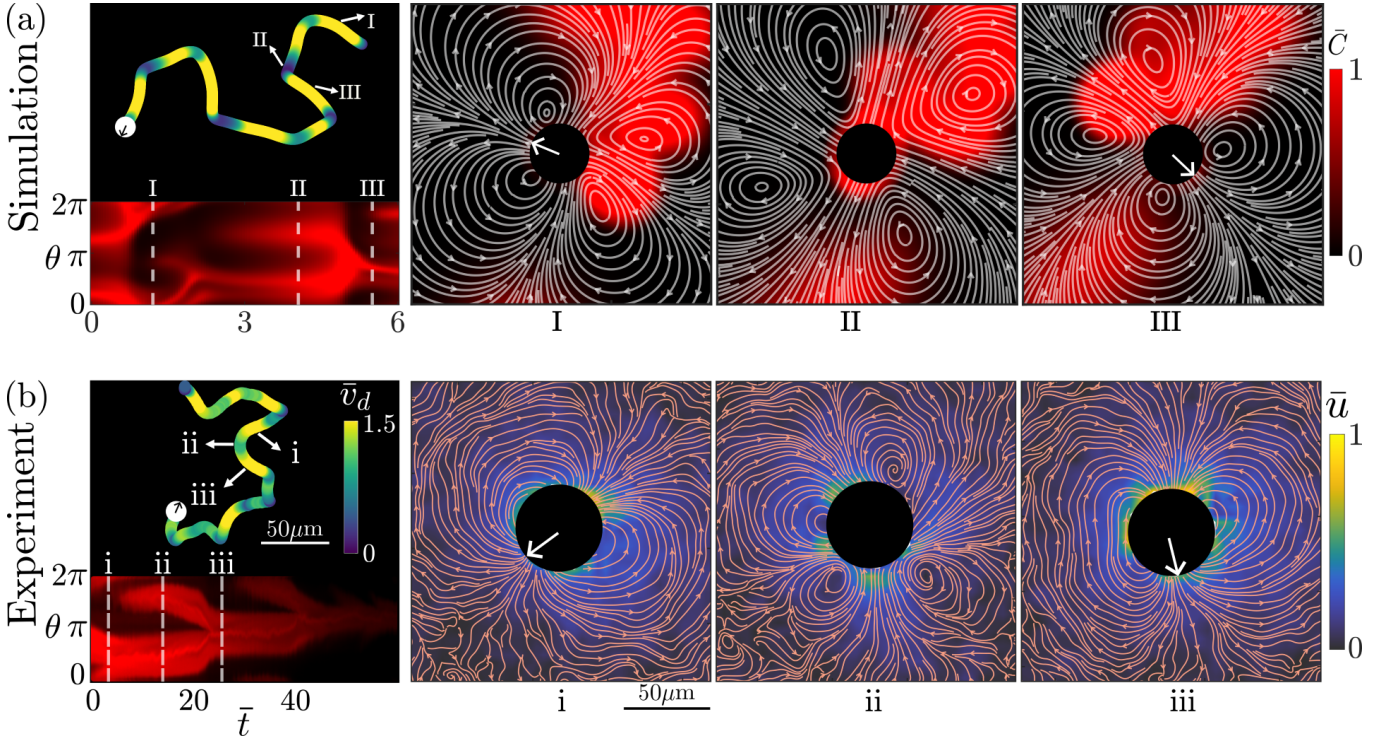
FIG. 5. **Chemical and hydrodynamic signatures at relatively large** Pe**.** (a) *Top row (Simulation)*: The microswimmer's trajectory, color-coded by non-dimensionalized propulsion speed $\bar{v}_d$, for Pe = 58, and the corresponding kymograph for the chemical concentration around the microswimmer's periphery over a portion of the trajectory. We have marked three instants in the trajectory and the kymograph over a typical reorientation event at large Pe– (I) an instant during which the microswimmer undergoes ballistic swimming prior to a local reorientation in the swimming direction, (II) an instant when the microswimmer is in a state of transient arrest, and (III) an instant when the microswimmer resumes its swimming following a reorientation event. The flow field (streamlines) generated by the microswimmer along with the corresponding distribution of the chemical concentration at each of the three instants are also shown here. (b) *Bottom row (Experiment):* The experimentally obtained trajectory of an active droplet for a comparable Pe = 50, along with the corresponding filled micelle kymograph over a part of the trajectory. The white circle representing the active droplet is not to scale. Here we have also marked three similar instants (i, ii, and iii) over a reorientation event as in the numerically obtained trajectory. The flow fields of the active droplet at these three instants are also shown separately using streamlines and the contour plots for the local flow speed ($\bar{u}$).

D. Chemo-hydrodynamic interactions at higher Péclet numbers

It is important to understand how our numerical simulation framework captures the aforementioned transition of the microswimmer dynamics to disordered (chaotic) motion with increasing Pe. With increasing viscosity, i.e. increasing Pe, two things get primarily altered– one, the strength of the stresslet contribution to the microswimmer disturbance field (Eq. 12) increases, and two, the diffusive time scale for the ejected chemical species increases, compared to the advective time scale, since $D(\nu)$ reduces with increasing ν. The increasing stresslet strength imparts the quadrupolar structure to the microswimmer flow field during its self-propulsion at higher Pe (Fig. 5(a)I), instead of the dipolar flow field at low Pe (Fig. 2(c); also see video S4). The transient dominance of the quadrupolar flow field (a symmetric quadrupolar structure) locally slows down the microswimmer, or even stalls it, while simultaneously pumping out the ejected chemical about the two locations on its periphery where it pumps out liquid (Fig. 5(a)II). The concentration of the ejected chemical does not undergo a diffusive relaxation, but is locally advected by the flow field since the diffusive time scale is longer than the advective time scale. This advection-dominated transport results in two branches of the chemical trail for the locally slowed down/stalled microswommer (instant II in the kymograph in Fig. 5(a)), instead of the one chemical branch observed during self-propulsion. Eventually, the chemical concentration around the microswimmer's periphery develops sufficient non-zero gradient to trigger renewed self-propulsion of the microswimmer along a direction different from its prior swimming orientation, and thereby undergoing a reorientation (compare Figs. 5(a)III and 5(a)I). Although the choice of the new swimming direction is non-deteriminstic in nature, it has to be along a direction where the microswimmer does not interact with its own chemical trail (preserved due to slow diffusion) because of its inherent anti-chemotactic nature. Note that at the onset of the renewed self-propulsion,

the two chemical branches again merge into a single posterior chemical wake (instant III in the kymograph in Fig. 5(a) and Fig. 5(a)III). The swimming continues until the quadrupolar contribution again slows down the microswimmer marking the onset of the next reorientation event. The fact that the dynamics of the microswimmer at higher Pe is dominated by the aforementioned reorientation events, which in turn are guided by the microswimmer's tendency to avoid its own chemical trail (chemotactic avoidance), results in the corresponding sub-ballistic scaling ($\propto \Delta \bar{t}^{1.5}$) for MSD at long times (Fig. 4(e)). Note that this scaling for MSD is compatible with self-avoiding random walk of active particles; an observation that has also been made experimentally for autophoretic microswimmers, like active droplets, at higher Pe [31].

The observations from the numerical simulations explained above are comparable to our experimental observations for the unsteady chemohydrodynamic characteristics of active droplets over a reorientation event at higher Pe (Fig. 5(b)). The active droplet shows similar dominance of the quadrupolar flow structure during a local arrest in the motion (Fig. 5(b)ii), along with the generation of two branches for the filled micelle concentration around its periphery (instant ii in kymograph in Fig. 5(b)). The new direction of swimming following the reorientation (Fig. 5(b)iii) is also in accordance with the anti-chemotactic nature of the active droplet. One point of difference to be noted here is that the active droplet exhibits a dipolar flow structure (Fig. 5(b)i and iii) during its self-propulsion instead of a quadrupolar flow field as in the numerical simulation (Fig. 5(a)I and III). This is because for the size of the droplet microswimmer used in the experimental system the resulting flow field during self-propulsion is dominated by the dipolar structure; experiments with a relatively smaller active droplet (but at the same Pe, which could have been achieved by adjusting the viscosity accordingly) would have shown a quadrupolar flow field during its self-propulsion (see supplementary material in [23]).

E. Pairwise interactions and chemotactic avoidance of autophoretic microswimmers

In this final subsection, we examine to what extent the numerical framework proposed here can capture the pairwise interaction of two autophoretic microswimmers. The simulations are performed at Pe ≈ 4, with two swimmers of the same radius a swimming in the same domain. When two microswimmers interact with each other, the steric repulsion in Eq. 11 becomes essential, preventing the swimmers from overlapping as they come close. Another key difference from the single-swimmer case is that during a pairwise interaction each swimmer can now interact with the hydrodynamic disturbance and the ejected chemical field created by the other. This chemo-hydrodynamic interaction significantly alters the swimming dynamics, and the velocities of the microswimmers are updated according to Eq. 10, capturing the details of the interaction.

Fig. 6, rows 1 and 2, show snapshots from the simulations that illustrate how two microswimmers interact with each other using chemical and hydrodynamic cues. In panels Fig. 6(a) and (c), the trajectories of the two swimmers are shown as they approach each other, 'sense' the others' chemical trail, and then turn away; also see video S5. In (a), the trajectory is overlaid on top of the chemical concentration field, while in (c) the trajectory is colour coded with $\bar{v}_d$. Initially, both swimmers swim following linear trajectories in a quasi-ballistic manner with comparable speeds (Fig. 6(c)) as explained before for low Péclet number. The chemical concentration distribution along with the streamlines, and the flow field during such an instant of approach are shown in Fig. 6 b(I) and d(I) respectively. Note that during such an instant, both microswimmers swim steadily with their chemical wake fixed at the rear apex, diametrically opposite to their swimming direction (Fig. 6 b(I)), as also discussed in Fig. 3(a). The microswimmmers also swim with a dipolar flow field (Fig. 6 d(I)) that is commensurate with the single-swimmer behaviour at the same Pe ≈ 4 (Fig. 2(c)). As the two microswimmers come closer to one another, each starts to interact with the chemical ejected by the other. At such an instant, both microswimmers slow down (instant II in Fig. 6(c), Fig. 6(b)II and (d)II), and simultaneously they begin to orient away from each other. Eventually, each swimmer gradually recovers its ballistic swimming, original swimming speed, and the dipolar flow field as they swim away from each other (instant III in Fig. 6(c), Fig. 6(b)III and (d)III). Note that the reorientation of the microswimmers cannot be due to long-range hydrodynamic interaction because the dipolar flow field created by the microswimmers is irrotational in nature. The reorientation of the microswimmers is solely due to the physical interaction of one microswimmer with the chemical wake emanating from the other. Hence, the numerical framework captures the anti-chemotactic nature of the autophoretic microswimmer leading to chemotactic avoidance.

The inferences from the numerical simulations as mentioned above are compatible with the observations from the experiments performed by us (Fig. 6 (bottom row)). Fig. 6(e) shows the trajectories of two active droplets color-coded by $\bar{v}_d$ during a pair-wise interaction. Note that, as observed in the simulations, the active droplet swimming with almost constant speed along a straight path slows down and changes its swimming direction (instant ii) when it encounters the chemical trail left behind by another active droplet. Eventually, the swimming speed of the active droplet gradually increases as it moves along the new direction, and it resumes quasi-ballistic swimming with a
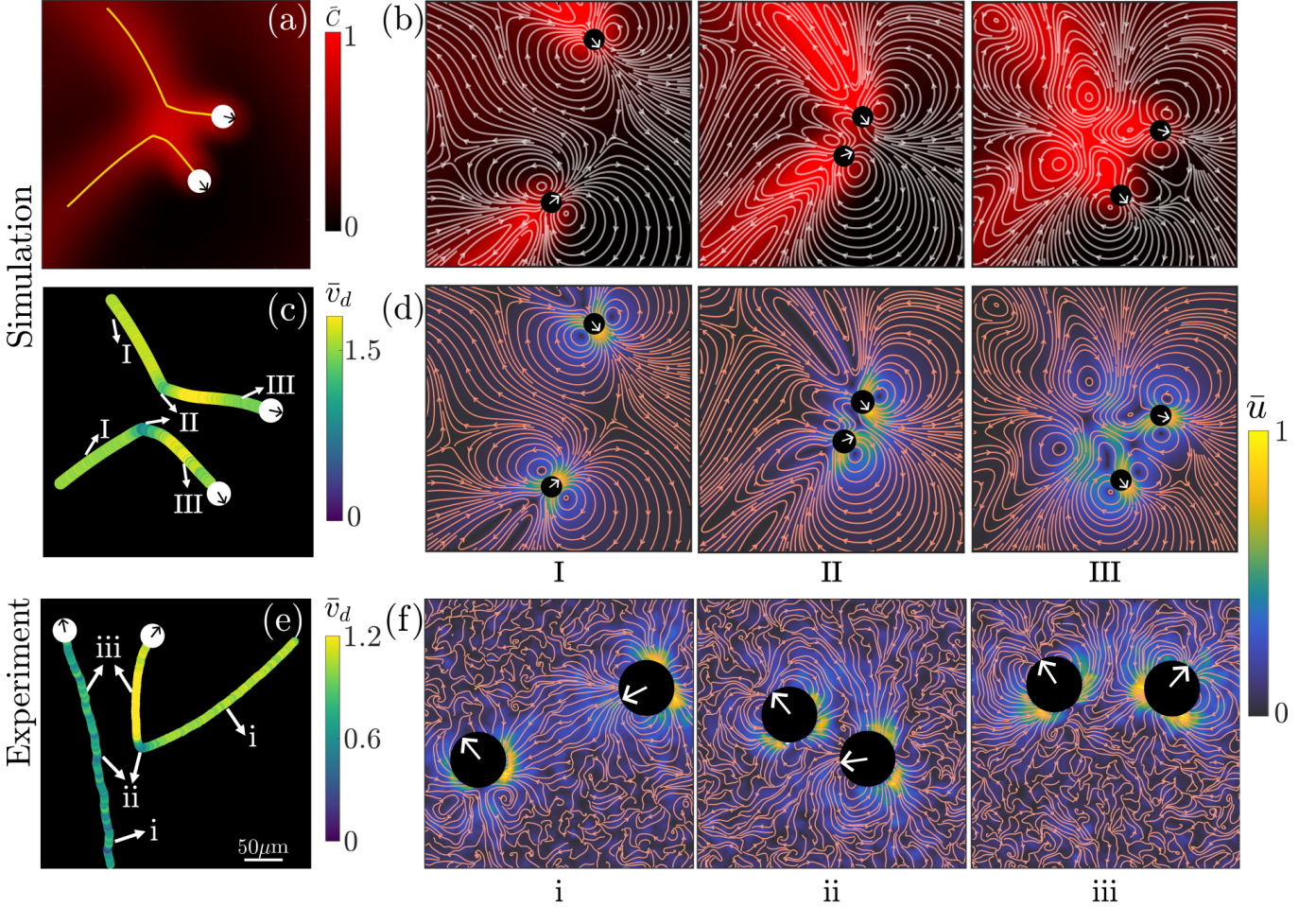
FIG. 6. **Pairwise interaction of active microswimmers at low viscosity, highlighting their chemotactic avoidance.** *Top two rows (Simulation):* (a) Trajectories of two microswimmers, overlaid on the chemical concentration distribution, as they swim towards one another. (c) The same trajectories color-coded by the non-dimensional swimming speed $\bar{v}_d$. Snapshots showing (b) the chemical concentration distribution along with the streamlines, and (d) the flow field in terms of the local flow speed $\bar{u}$ and streamlines at three different instants– (I) as the two microswimmers approach each other, (II) at the instant of their closest approach, and (III) after the microswimmers move away from each other. *Bottom row (Experiment):* (e) Experimental results showing the interaction between two active droplets. (f) Flow fields taken at corresponding moments (i–iii) show a similar sequence of interactions as observed in the numerical simulations.

dipolar flow field (instant iii). Since our numerical framework can capture the chemotactic avoidance of autophoretic microswimmers like active droplets, we think that it will be able to recreate/predict the collective behaviour of such microswimmers stemming from chemo-hydrodynamic ineractions [30].

V. CONCLUDING REMARKS

Our numerical framework provides a self-consistent description of the swimming dynamics of autophoretic microswimmers, in which the chemical concentration field, velocity at the surface of the microswimmer (slip velocity), hydrodynamic signature of the microswimmer, and particle motion coevolve. The proposed numerical framework has the following advantageous featrues–

(i) the chemical source is defined at the microswimmer's center and smoothly distributed over the domain using a hyperbolic tangent profile. This lets us evolve the chemical field by solving a single advection–diffusion equation on a fixed grid, without imposing the flux conditions on the moving surface. This avoids explicit moving-boundary treatment and improves numerical stability. Hence, the slip velocity comes from the concentration differences on the particle surface, so interactions between many particles can be captured naturally without approximations.

(ii) in the proposed model the disturbance triggered by the microswimmer, i.e. the strength of the stresslet, is not

prescribed a priori; instead, both the slip velocity and the stresslet emerge consistently from the evolving chemical field distribution around the microswimmer. As a result, the strength and direction of the stresslet adjust spontaneously at every time step, capturing the coupled interaction between the chemical transport and the surrounding flow field. (iii) at the same time, the finite size of the microswimmer is included in the modeling framework in a simple way by spreading the computed stresslet smoothly around the particle's centre using a Gaussian envelope. This method circumvents treating the swimmer as a point-like particle, and allows it to generate a hydrodynamic signature that is realistic even in its near-field features as established through comparison with experiments. The smoothly distributed stress is added as a body force in the momentum equation. The numerical framework then updates the full Navier–Stokes equations with this extra forcing at every time step.

At low Péclet numbers, the essential features of the swimming dynamics, like swimming trajectory, orientation, and hydrodynamic signature are in good agreement with the experiments performed with active droplets. Quantitative measures such as mean-squared displacement, angular autocorrelation, and local flow speeds further confirm that the simulations accurately capture the swimming characteristics of the autophoretic microswimmers. Additionally, the simulations also show that the microswimmer swims steadily by leaving behind a uniform chemical trail which is fixed at the rear apex of the microswimmer, diametrically opposite to its swimming direction. The spatio-temporal evolution of this self-generated chemical trail in the swimming medium is diffusive in nature, which is consistent with the experimental observations concerning the filled micelle trail left behind by active droplets.

By choosing the diffusion strength of the ejected chemical to vary inversely with the viscosity of the swimming medium, the model consistently captures the corresponding variations in the Péclet number. As the Péclet number is increased, the swimmer exhibits reduced directional stability and increasingly disturbed motion- a trend which is also observed in our experiments and has been established in the literature [31, 68]. This transition in the swimming dynamics is reflected in the swimming trajectory and in a broader distribution of non-dimensionalised propulsion speed. The mean-squared displacement transitions from ballistic to sub-ballistic scaling consistent with self-avoiding random walk, indicating a gradual loss of persistent motion. A key point to be noted here is that the angular autocorrelation behaves non-monotonically— with increasing Péclet number first the autocorrelation function decays faster as the swimmer reorients more often, but beyond a certain Péclet number the decay becomes slower as the microswimmer stalls more frequently. In contrast, the velocity autocorrelation decreases monotonically with increasing Péclet number denoting a loss of short-time velocity memory. Our numerical framework captures the dominance of the quadrupolar flow field with increasing Péclet number and the associated advection-driven transport of the ejected chemical species. This feature, coupled with the anti-chemotactic nature of the simulated microswimmer in-built into the framework, remarkably captures the emergent disordered motion of the microswimmer with increasing Pe. The numerical simulation consistently captures the switching between hydrodynamic signatures and the chemical concentration distribution over a reorientation event which is a hallmark of the dynamics at high Pe as demonstrated in the existing literature [31] and by our own experiments.

The ability of our simulation to preserve a memory of the microswimmer's trajectory by consistently evolving the chemical trail, along with the anti-chemotactic nature of the simulated microswimmer, help to closely mimic the pairwise interaction of autophoretic microswimmers as demonstrated in the literature [30] and by our experiments using active droplets. Specifically, the simulations closely reproduce the trail avoidance behaviour where a microswimmer responds to the chemical field of another microswimmer by steering away from it. Hence, our numerical simulation can successfully capture chemical-cue-based signalling that could play an important role in collective behaviour. Although the hydrodynamic boundary condition for the autophoretic microswimmer implemented in the numerical framework is the phoretic slip condition, the numerical results closely mimic the experimental observations using active droplets which satisfy the Marangoni stress boundary condition at its interface. This further establishes the generality of the proposed numerical modeling technique for autophoretic microswimmers.

This model also provides a versatile platform to explore the dynamics of autophoretic microswimmers at multiple scales. For individual swimmers, it allows for systematic variation of key parameters, such as microswimmer size, chemical activity, and swimming strength, over a wide range which may not be trivially accessible by experiments, enabling a detailed understanding of how these factors influence swimming characteristics. The framework can be extended to simulate the emergent collective behaviour of many interacting microswimmers. Experiments have observed collective effects such as self-induced caging [30] and dynamic clustering in systems of chemically active particles [32, 45]; our numerical framework can be used to simulate and better understand such collective behaviour. In fact, our numerical model can probe deeper towards investigating how local interactions lead to dynamic clustering, coordinated alignment, large-scale motion, and emergent transport patterns in crowded or confined environments. By varying parameters like microswimmer density, Péclet number, and chemical interactions, the simulations can provide quantitative predictions of velocity correlations, spatio-temporal organization, and other signatures of emergent collective behavior, complementing and extending experimental insights while opening new avenues for exploring active matter.

VI. SUPPLEMENTARY VIDEOS

1. Numerical simulation and experiments illustrating the dynamics of the microswimmer at low Péclet number. Ist quadrant: trajectory of the microswimmer color-coded with instantaneous velocity, IInd quadrant: visualization of the chemical trail as the droplet swims, evaluated using numerical model at Pe = 6; IIIrd quadrant: experimental visualization of the chemical trail, IVth quadrant: experimental trajectory of the microswimmer color-coded with instantaneous velocity at Pe = 4, for video click video S1.

2. Numerical simulation and experiments illustrating the dynamics of the microswimmer at intermediate Péclet number. Ist quadrant: trajectory of the microswimmer color-coded with instantaneous velocity, IInd quadrant: visualization of the chemical trail as the droplet swims, evaluated using numerical model at Pe = 35; IIIrd quadrant: experimental visualization of the chemical trail, IVth quadrant: experimental trajectory of the microswimmer color-coded with instantaneous velocity at Pe = 15. For video click video S2

3. Numerical simulation and experiments illustrating the dynamics of the microswimmer at the high Péclet number. Ist quadrant: trajectory of the microswimmer color-coded with instantaneous velocity, IInd quadrant: visualization of the chemical trail as the droplet swims, evaluated using numerical model at Pe = 254; IIIrd quadrant: experimental visualization of the chemical trail, IVth quadrant: experimental trajectory of the microswimmer color-coded with instantaneous velocity at Pe = 50. For video click video S3

4. Change in the hydrodynamic signature of the microswimmer at high Péclet number. Left panel: Streamlines (flow field) around the microswimmer plotted on top of the chemical trail, using the numerical model at Pe = 58. Right panel: Streamlines (flow field) around the microswimmer plotted on top of the magnitude of the generated flow field using experiments at Pe = 50. For video click video S4

5. Numerical simulation and experiments illustrating the chemotactic avoidance of the microswimmer at low Péclet number. Ist quadrant: trajectory of the microswimmers color-coded with instantaneous velocity, IInd quadrant: visualization of change in the direction of swimming of the microswimer due to chemotactic signal from another microswimmer, evaluated using the numerical model at Pe = 4; IIIrd quadrant: experimental visualization of change in the direction of swimming due to chemotactic signal from another microswimmer, IVth quadrant: experimental trajectory of the microswimmers, color-coded with instantaneous velocity at Pe = 4. For video click video S5

All videos are playing at 25fps. The videos are compiled using ImageJ [81].

------

* ph20resch11020@iith.ac.in
† ranabir@mae.iith.ac.in
‡ agupta@phy.iith.ac.in

[1] ANDERSON, J. L. 1989 Colloid transport by interfacial forces. *Annual Review of Fluid Mechanics* **21**, 61–99.
[2] BAN, TAKAHIKO, SUGIYAMA, MICHIAKI, NAGATSU, YUICHIRO & TOKUYAMA, HIDEAKI 2018 Motion-based detection of lanthanides (iii) using self-propelled droplets. *The Journal of Physical Chemistry B* **122** (46), 10647–10651.

[3] BATCHELOR, GK 1970 The stress system in a suspension of force-free particles. *Journal of fluid mechanics* **41** (3), 545–570.

[4] BIRRER, SAMUEL, CHEON, SEONG IK & ZARZAR, LAUREN D 2022 We the droplets: a constitutional approach to active and self-propelled emulsions. *Current Opinion in Colloid & Interface Science* **61**, 101623.

[5] BUNEA, ADA-IOANA, MARTELLA, DANIELE, NOCENTINI, SARA, PARMEGGIANI, CAMILLA, TABORYSKI, RAFAEL & WIERSMA, DIEDERIK S 2021 Light-powered microrobots: challenges and opportunities for hard and soft responsive microswimmers. *Advanced Intelligent Systems* **3** (4), 2000256.

[6] BUNEA, ADA-IOANA & TABORYSKI, RAFAEL 2020 Recent advances in microswimmers for biomedical applications. *Micromachines* **11** (12), 1048.

[7] CAMPBELL, ANDREW I, EBBENS, STEPHEN J, ILLIEN, PIERRE & GOLESTANIAN, RAMIN 2019 Experimental observation of flow fields around active janus spheres. *Nature Communications* **10** (1), 3952.

[8] CANTISÁN, JULIA, SEOANE, JESÚS M & SANJUÁN, MIGUEL AF 2023 Rotating cluster formations emerge in an ensemble of active particles. *Chaos, Solitons & Fractals* **172**, 113531.

[9] CANUTO, CLAUDIO, HUSSAINI, M YOUSSUFF, QUARTERONI, ALFIO & ZANG, THOMAS A 2006 *Spectral methods: fundamentals in single domains*. Springer.

[10] CHESSHIRE, G & HENSHAW, WILLIAM D 1990 Composite overlapping meshes for the solution of partial differential equations. *Journal of Computational Physics* **90** (1), 1–64.

[11] CS, PESKIN 2002 The immersed boundary method. *Acta Nuerica* **11**, 479–517.

[12] DELMOTTE, BLAISE & USABIAGA, FLORENCIO BALBOA 2024 A scalable method to model large suspensions of colloidal phoretic particles with arbitrary shapes. *Journal of Computational Physics* **518**, 113321.

[13] DESAI, NIKHIL & MICHELIN, SÉBASTIEN 2021 Instability and self-propulsion of active droplets along a wall. *Physical Review Fluids* **6** (11), 114103.

[14] DWIVEDI, PRATEEK, SI, BISHWA RANJAN, PILLAI, DIPIN & MANGAL, RAHUL 2021 Solute induced jittery motion of self-propelled droplets. *Physics of Fluids* **33** (2).

[15] EBBENS, STEPHEN J & GREGORY, DAVID ALEXANDER 2018 Catalytic janus colloids: controlling trajectories of chemical microswimmers. *Accounts of chemical research* **51** (9), 1931–1939.

[16] EBRAHIMI, NAFISEH, BI, CHENGHAO, CAPPELLERI, DAVID J, CIUTI, GASTONE, CONN, ANDREW T, FAIVRE, DAMIEN, HABIBI, NEDA, HOŠOVSKÝ, ALEXANDER, IACOVACCI, VERONICA, KHALIL, ISLAM SM & OTHERS 2021 Magnetic actuation methods in bio/soft robotics. *Advanced Functional Materials* **31** (11), 2005137.

[17] FARUTIN, ALEXANDER, RIZVI, MOHD SUHAIL, HU, W-F, LIN, TE SHENG, RAFAI, SALIMA & MISBAH, CHAOUQI 2022 A reduced model for a phoretic swimmer. *Journal of Fluid Mechanics* **952**, A6.

[18] FEDOSOV, DMITRY A, CASWELL, BRUCE & KARNIADAKIS, GEORGE EM 2010 A multiscale red blood cell model with accurate mechanics, rheology, and dynamics. *Biophysical journal* **98** (10), 2215–2225.

[19] FRIGO, MATTEO & JOHNSON, STEVEN G 2005 The design and implementation of fftw3. *Proceedings of the IEEE* **93** (2), 216–231.

[20] GHOSH, AMBARISH & FISCHER, PEER 2009 Controlled propulsion of artificial magnetic nanostructured propellers. *Nano letters* **9** (6), 2243–2245.

[21] GOLESTANIAN, RAMIN, LIVERPOOL, TB & AJDARI, A 2007 Designing phoretic micro-and nano-swimmers. *New Journal of Physics* **9** (5), 126.

[22] GOU, ZHE, MISBAH, CHAOUQI & FARUTIN, ALEXANDER 2025 A computational framework for simulating suspensions of phoretic particles. *Journal of Fluid Mechanics* **1016**, A25.

[23] GUCHHAIT, SUBHASISH, SONTAKKE, SMITA S, MANDAL, SHUBHADEEP & DEY, RANABIR 2025 Flow fields around active droplets squeezing through tight confinements. *Physical Review Fluids* **10** (4), 044202.

[24] GUPTA, ANUPAM, MAGAUD, PASCALE, LAFFORGUE, CHRISTINE & ABBAS, MICHELINE 2018 Conditional stability of particle alignment in finite-reynolds-number channel flow. *Physical Review Fluids* **3** (11), 114302.

[25] GUPTA, ANUPAM, VINCENZI, DARIO & PANDIT, RAHUL 2014 Elliptical tracers in two-dimensional, homogeneous, isotropic fluid turbulence: The statistics of alignment, rotation, and nematic order. *Physical Review E* **89** (2), 021001.

[26] HAN, ENDAO, ZHU, LAILAI, SHAEVITZ, JOSHUA W & STONE, HOWARD A 2021 Low-reynolds-number, biflagellated quincke swimmers with multiple forms of motion. *Proceedings of the National Academy of Sciences* **118** (29), e2022000118.

[27] HAN, KOOHEE, SHIELDS IV, C WYATT & VELEV, ORLIN D 2018 Engineering of self-propelling microbots and microdevices powered by magnetic and electric fields. *Advanced Functional Materials* **28** (25), 1705953.

[28] HENSHAW, WILLIAM D & SCHWENDEMAN, DONALD W 2008 Parallel computation of three-dimensional flows using overlapping grids with adaptive mesh refinement. *Journal of Computational Physics* **227** (16), 7469–7502.

[29] HERMINGHAUS, STEPHAN, MAASS, CORINNA C, KRÜGER, CARSTEN, THUTUPALLI, SHASHI, GOEHRING, LUCAS & BAHR, CHRISTIAN 2014 Interfacial mechanisms in active emulsions. *Soft Matter* **10** (36), 7008–7022.

[30] HOKMABAD, BABAK VAJDI, AGUDO-CANALEJO, JAIME, SAHA, SUROPRIYA, GOLESTANIAN, RAMIN & MAASS, CORINNA C 2022 Chemotactic self-caging in active emulsions. *Proceedings of the National Academy of Sciences* **119** (24), e2122269119.

[31] HOKMABAD, BABAK VAJDI, DEY, RANABIR, JALAAL, MAZIYAR, MOHANTY, DEVADITYA, ALMUKAMBETOVA, MADINA, BALDWIN, KYLE A, LOHSE, DETLEF & MAASS, CORINNA C 2021 Emergence of bimodal motility in active droplets. *Physical review X* **11** (1), 011043.

[32] HOKMABAD, BABAK VAJDI, NISHIDE, AKINORI, RAMESH, PRASHANTH, KRÜGER, CARSTEN & MAASS, CORINNA C 2022 Spontaneously rotating clusters of active droplets. *Soft matter* **18** (14), 2731–2741.

[33] HOOGERBRUGGE, PJ & KOELMAN, JOHANNES MVA 1992 Simulating microscopic hydrodynamic phenomena with dissipative particle dynamics. *Europhysics letters* **19** (3), 155.

[34] HOSSEINI, S MAJID & FENG, JAMES J 2009 A particle-based model for the transport of erythrocytes in capillaries. *Chemical engineering science* **64** (22), 4488–4497.

[35] Howse, Jonathan R, Jones, Richard AL, Ryan, Anthony J, Gough, Tim, Vafabakhsh, Reza & Golestanian, Ramin 2007 Self-motile colloidal particles: from directed propulsion to random walk. *Physical Review Letters* **99** (4), 048102.

[36] Hu, Wei-Fan, Lin, Te-Sheng, Rafai, Salima & Misbah, Chaouqi 2019 Chaotic swimming of phoretic particles. *Physical review letters* **123** (23).

[37] Illien, Pierre, Golestanian, Ramin & Sen, Ayusman 2017 'fuelled'motion: phoretic motility and collective behaviour of active colloids. *Chemical Society Reviews* **46** (18), 5508–5518.

[38] Ishikawa, Takuji, Sekiya, Go, Imai, Yohsuke & Yamaguchi, Takami 2007 Hydrodynamic interactions between two swimming bacteria. *Biophysical journal* **93** (6), 2217–2225.

[39] Izri, Ziane, Van Der Linden, Marjolein N, Michelin, Sébastien & Dauchot, Olivier 2014 Self-propulsion of pure water droplets by spontaneous marangoni-stress-driven motion. *Physical review letters* **113** (24), 248302.

[40] Izzet, Adrien, Moerman, Pepijn G, Gross, Preston, Groenewold, Jan, Hollingsworth, Andrew D, Bibette, Jérôme & Brujic, Jasna 2020 Tunable persistent random walk in swimming droplets. *Physical Review X* **10** (2), 021035.

[41] Jin, Chenyu, Vachier, Jérémy, Bandyopadhyay, Soumya, Macharashvili, Tamara & Maass, Corinna C 2019 Fine balance of chemotactic and hydrodynamic torques: When microswimmers orbit a pillar just once. *Physical Review E* **100** (4), 040601.

[42] Joh, Hyungmok & Fan, Donglei Emma 2021 Materials and schemes of multimodal reconfigurable micro/nanomachines and robots: review and perspective. *Advanced Materials* **33** (39), 2101965.

[43] Kagan, Daniel, Laocharoensuk, Rawiwan, Zimmerman, Maria, Clawson, Corbin, Balasubramanian, Shankar, Kang, Dae, Bishop, Daniel, Sattayasamitsathit, Sirilak, Zhang, Liangfang & Wang, Joseph 2010 Rapid delivery of drug carriers propelled and navigated by catalytic nanoshuttles. *Small* **6** (23), 2741–2747.

[44] Katuri, Jaideep, Ma, Xing, Stanton, Morgan M & Sánchez, Samuel 2017 Designing micro-and nanoswimmers for specific applications. *Accounts of chemical research* **50** (1), 2–11.

[45] Krueger, Carsten, Bahr, Christian, Herminghaus, Stephan & Maass, Corinna C 2016 Dimensionality matters in the collective behaviour of active emulsions. *The European Physical Journal E* **39** (6), 64.

[46] Krüger, Carsten, Klös, Gunnar, Bahr, Christian & Maass, Corinna C 2016 Curling liquid crystal microswimmers: A cascade of spontaneous symmetry breaking. *Physical Review Letters* **117** (4), 048003.

[47] Kumar, Manoj, Murali, Aniruddh, Subramaniam, Arvin Gopal, Singh, Rajesh & Thutupalli, Shashi 2024 Emergent dynamics due to chemo-hydrodynamic self-interactions in active polymers. *Nature Communications* **15** (1), 4903.

[48] Lauga, Eric & Michelin, Sébastien 2016 Stresslets induced by active swimmers. *Physical Review Letters* **117** (14), 148001.

[49] Li, Wanyuan, Wu, Changjin, Xiong, Ze, Liang, Chaowei, Li, Ziyi, Liu, Baiyao, Cao, Qinyi, Wang, Jizhuang, Tang, Jinyao & Li, Dan 2022 Self-driven magnetorobots for recyclable and scalable micro/nanoplastic removal from nonmarine waters. *Science Advances* **8** (45), eade1731.

[50] Liebchen, Benno & Mukhopadhyay, Aritra K 2021 Interactions in active colloids. *Journal of Physics: Condensed Matter* **34** (8), 083002.

[51] Lippera, Kevin, Benzaquen, Michael & Michelin, Sébastien 2021 Alignment and scattering of colliding active droplets. *Soft Matter* **17** (2), 365–375.

[52] Lippera, Kevin, Morozov, Matvey, Benzaquen, Michael & Michelin, Sébastien 2020 Collisions and rebounds of chemically active droplets. *Journal of Fluid Mechanics* **886**, A17.

[53] Lomholt, Sune & Maxey, Martin R 2003 Force-coupling method for particulate two-phase flow: Stokes flow. *Journal of Computational Physics* **184** (2), 381–405.

[54] Lushi, Enkeleida & Peskin, Charles S 2013 Modeling and simulation of active suspensions containing large numbers of interacting micro-swimmers. *Computers & Structures* **122**, 239–248.

[55] Lushi, Enkeleida, Wioland, Hugo & Goldstein, Raymond E 2014 Fluid flows created by swimming bacteria drive self-organization in confined suspensions. *Proceedings of the National Academy of Sciences* **111** (27), 9733–9738.

[56] Ma, Kun, Xu, Shuai, Tao, Tongxiang, Qian, Junchao, Cui, Qiqi, Rehman, Sajid ur, Zhu, Xiaoguang, Chen, Ruiguo, Zhao, Hongxin, Wang, Changhao & others 2022 Magnetosome-inspired synthesis of soft ferrimagnetic nanoparticles for magnetic tumor targeting. *Proceedings of the National Academy of Sciences* **119** (45), e2211228119.

[57] Maass, Corinna C, Krüger, Carsten, Herminghaus, Stephan & Bahr, Christian 2016 Swimming droplets. *Annual Review of Condensed Matter Physics* **7** (1), 171–193.

[58] Martín-Roca, José, Ortega, Francisco, Valeriani, Chantal, Rubio, Ramón González & Martínez-Pedrero, Fernando 2023 Magnetic colloidal currents guided on self-assembled colloidal tracks. *Advanced Functional Materials* **33** (52), 2306541.

[59] Maxey, MR & Patel, BK 2001 Localized force representations for particles sedimenting in stokes flow. *International journal of multiphase flow* **27** (9), 1603–1626.

[60] McCorquodale, Peter, Colella, Phillip & Johansen, Hans 2001 A cartesian grid embedded boundary method for the heat equation on irregular domains. *Journal of Computational Physics* **173** (2), 620–635.

[61] Merrill, Brandon E & Peet, Yulia T 2019 Moving overlapping grid methodology of spectral accuracy for incompressible flow solutions around rigid bodies in motion. *Journal of Computational Physics* **390**, 121–151.

[62] Michelin, Sébastien 2023 Self-propulsion of chemically active droplets. *Annual Review of Fluid Mechanics* **55** (1), 77–101.

[63] Michelin, Sébastien & Lauga, Eric 2014 Phoretic self-propulsion at finite péclet numbers. *Journal of fluid mechanics* **747**, 572–604.

[64] MICHELIN, SÉBASTIEN, LAUGA, ERIC & BARTOLO, DENIS 2013 Spontaneous autophoretic motion of isotropic particles. *Physics of Fluids* **25** (6).

[65] MOERMAN, PEPIJN G, MOYSES, HENRIQUE W, VAN DER WEE, ERNEST B, GRIER, DAVID G, VAN BLAADEREN, ALFONS, KEGEL, WILLEM K, GROENEWOLD, JAN & BRUJIC, JASNA 2017 Solute-mediated interactions between active droplets. *Physical Review E* **96** (3), 032607.

[66] MONAGHAN, J. J. 1994 Simulating free surface flows with sph. *Journal of Computational Physics* **110**, 399–406.

[67] MORAN, JEFFREY L & POSNER, JONATHAN D 2017 Phoretic self-propulsion. *Annual Review of Fluid Mechanics* **49** (1), 511–540.

[68] MOROZOV, MATVEY & MICHELIN, SÉBASTIEN 2019 Nonlinear dynamics of a chemically-active drop: from steady to chaotic self-propulsion. *The Journal of chemical physics* **150** (4).

[69] MOROZOV, MATVEY & MICHELIN, SÉBASTIEN 2019 Self-propulsion near the onset of marangoni instability of deformable active droplets. *Journal of Fluid Mechanics* **860**, 711–738.

[70] NOGUCHI, HIROSHI & GOMPPER, GERHARD 2004 Fluid vesicles with viscous membranes in shear flow. *Physical review letters* **93** (25), 258102.

[71] NOGUCHI, HIROSHI & GOMPPER, GERHARD 2005 Shape transitions of fluid vesicles and red blood cells in capillary flows. *Proceedings of the National Academy of Sciences* **102** (40), 14159–14164.

[72] ORSZAG, STEVEN A 1971 On the elimination of aliasing in finite-difference schemes by filtering high-wavenumber components. *Journal of Atmospheric Sciences* **28** (6), 1074–1074.

[73] PANDIT, RAHUL, BANERJEE, DEBARGHYA, BHATNAGAR, AKSHAY, BRACHET, MARC, GUPTA, ANUPAM, MITRA, DHRUBADITYA, PAL, NAIRITA, PERLEKAR, PRASAD, RAY, SAMRIDDHI SANKAR, SHUKLA, VISHWANATH & OTHERS 2017 An overview of the statistical properties of two-dimensional turbulence in fluids with particles, conducting fluids, fluids with polymer additives, binary-fluid mixtures, and superfluids. *Physics of fluids* **29** (11).

[74] PAXTON, WALTER F, KISTLER, KEVIN C, OLMEDA, CHRISTINE C, SEN, AYUSMAN, ST. ANGELO, SARAH K, CAO, YANYAN, MALLOUK, THOMAS E, LAMMERT, PAUL E & CRESPI, VINCENT H 2004 Catalytic nanomotors: autonomous movement of striped nanorods. *Journal of the American Chemical Society* **126** (41), 13424–13431.

[75] PEDDIREDDY, KARTHIK, KUMAR, PRAMODA, THUTUPALLI, SHASHI, HERMINGHAUS, STEPHAN & BAHR, CHRISTIAN 2012 Solubilization of thermotropic liquid crystal compounds in aqueous surfactant solutions. *Langmuir* **28** (34), 12426–12431.

[76] PERLEKAR, PRASAD, RAY, SAMRIDDHI SANKAR, MITRA, DHRUBADITYA & PANDIT, RAHUL 2011 Persistence problem in two-dimensional fluid turbulence. *Physical review letters* **106** (5), 054501.

[77] PICELLA, FRANCESCO & MICHELIN, SÉBASTIEN 2022 Confined self-propulsion of an isotropic active colloid. *Journal of Fluid Mechanics* **933**, A27.

[78] POZRIKIDIS, CONSTANTINE 1992 *Boundary integral and singularity methods for linearized viscous flow*. Cambridge university press.

[79] PRESS, WILLIAM H 2007 *Numerical recipes 3rd edition: The art of scientific computing*. Cambridge university press.

[80] PREWITT, NATHAN C, BELK, DAVY M & SHYY, WEI 2000 Parallel computing of overset grids for aerodynamic problems with moving objects. *Progress in Aerospace Sciences* **36** (2), 117–172.

[81] SCHNEIDER, CAROLINE A, RASBAND, WAYNE S & ELICEIRI, KEVIN W 2012 Nih image to imagej: 25 years of image analysis. *Nature Methods* **9** (7), 671–675.

[82] SCHNEIDERS, LENNART, GÜNTHER, CLAUDIA, MEINKE, MATTHIAS & SCHRÖDER, WOLFGANG 2016 An efficient conservative cut-cell method for rigid bodies interacting with viscous compressible flows. *Journal of Computational Physics* **311**, 62–86.

[83] SINGH, RAJESH, ADHIKARI, R & CATES, ME 2019 Competing chemical and hydrodynamic interactions in autophoretic colloidal suspensions. *The Journal of chemical physics* **151** (4).

[84] SOLOMON, TH & MEZIĆ, IGOR 2003 Uniform resonant chaotic mixing in fluid flows. *Nature* **425** (6956), 376–380.

[85] STONE, HOWARD A & SAMUEL, ARAVINTHAN DT 1996 Propulsion of microorganisms by surface distortions. *Physical review letters* **77** (19), 4102.

[86] SU, HAIYANG, PRICE, C-A HURD, JING, LINGYAN, TIAN, QIANG, LIU, JIAN & QIAN, KUN 2019 Janus particles: design, preparation, and biomedical applications. *Materials today bio* **4**, 100033.

[87] SUGA, MARIKO, SUDA, SAORI, ICHIKAWA, MASATOSHI & KIMURA, YASUYUKI 2018 Self-propelled motion switching in nematic liquid crystal droplets in aqueous surfactant solutions. *Physical Review E* **97** (6), 062703.

[88] SUNDARARAJAN, SHAKUNTALA, LAMMERT, PAUL E, ZUDANS, ANDREW W, CRESPI, VINCENT H & SEN, AYUSMAN 2008 Catalytic motors for transport of colloidal cargo. *Nano letters* **8** (5), 1271–1276.

[89] TANAKA, NOBUATSU & TAKANO, TATSUO 2005 Microscopic-scale simulation of blood flow using sph method. *International Journal of Computational Methods* **2** (04), 555–568.

[90] THIELICKE, WILLIAM & STAMHUIS, EIZE 2014 Pivlab–towards user-friendly, affordable and accurate digital particle image velocimetry in matlab. *Journal of open research software* **2** (1), 30.

[91] THOMASES, BECCA & SHELLEY, MICHAEL 2009 Transition to mixing and oscillations in a stokesian viscoelastic flow. *Physical review letters* **103** (9), 094501.

[92] THUTUPALLI, SHASHI, GEYER, DELPHINE, SINGH, RAJESH, ADHIKARI, RONOJOY & STONE, HOWARD A 2018 Flow-induced phase separation of active particles is controlled by boundary conditions. *Proceedings of the National Academy of Sciences* **115** (21), 5403–5408.

[93] THUTUPALLI, SHASHI, SEEMANN, RALF & HERMINGHAUS, STEPHAN 2011 Swarming behavior of simple model squirmers. *New Journal of Physics* **13** (7), 073021.

[94] TIERNO, PIETRO, GOLESTANIAN, RAMIN, PAGONABARRAGA, IGNACIO & SAGUÉS, FRANCESC 2008 Magnetically actuated colloidal microswimmers. *The Journal of Physical Chemistry B* **112** (51), 16525–16528.

[95] TOYOTA, TARO, MARU, NAOTO, HANCZYC, MARTIN M, IKEGAMI, TAKASHI & SUGAWARA, TADASHI 2009 Self-propelled oil droplets consuming "fuel" surfactant. *Journal of the American Chemical Society* **131** (14), 5012–5013.

[96] VARMA, AKHIL, MONTENEGRO-JOHNSON, THOMAS D & MICHELIN, SÉBASTIEN 2018 Clustering-induced self-propulsion of isotropic autophoretic particles. *Soft matter* **14** (35), 7155–7173.

[97] VELEGOL, DARRELL, GARG, ASTHA, GUHA, RAJARSHI, KAR, ABHISHEK & KUMAR, MANISH 2016 Origins of concentration gradients for diffusiophoresis. *Soft matter* **12** (21), 4686–4703.

[98] WANG, XIAOLONG, GONG, XIAOBO, SUGIYAMA, KAZUYASU, TAKAGI, SHU & HUANG, HUAXIONG 2020 An immersed boundary method for mass transfer through porous biomembranes under large deformations. *Journal of Computational Physics* **413**, 109444.

[99] XU, ZHIKE, WANG, CHENYANG, HE, FENG, HAO, PENGFEI & ZHANG, XIWEN 2023 Coarse-grained model of whole blood hemolysis and morphological analysis of erythrocyte population under non-physiological shear stress flow environment. *Physics of Fluids* **35** (3).

[100] YANG, QIANHONG, JIANG, MAOQIANG, PICANO, FRANCESCO & ZHU, LAILAI 2024 Shaping active matter from crystalline solids to active turbulence. *Nature Communications* **15** (1), 2874.

[101] ZHANG, JIE, GRZYBOWSKI, BARTOSZ A & GRANICK, STEVE 2017 Janus particle synthesis, assembly, and application. *Langmuir* **33** (28), 6964–6977.

[102] ZHANG, JING, ZHENG, XU, CUI, HAIHANG & SILBER-LI, ZHANHUA 2017 The self-propulsion of the spherical pt–sio2 janus micro-motor. *Micromachines* **8** (4), 123.

[103] ZÖTTL, ANDREAS & STARK, HOLGER 2016 Emergent behavior in active colloids. *Journal of Physics: Condensed Matter* **28** (25), 253001.

[104] ZÖTTL, ANDREAS & STARK, HOLGER 2023 Modeling Active Colloids: From Active Brownian Particles to Hydrodynamic and Chemical Fields. *Annual Review of Condensed Matter Physics* **14** (1), 109–127.